



Synthesis of NiMo catalysts supported on mesoporous Al-SBA-15 with different morphologies and their catalytic performance of DBT HDS



Daowei Gao^a, Aijun Duan^{a,*}, Xin Zhang^{a,*}, Zhen Zhao^a, Hong E^a, Jianmei Li^b, Hai Wang^c

^a State Key Laboratory of Heavy Oil Processing, China University of Petroleum, Beijing 102249, PR China

^b College of Science, China University of Petroleum, Beijing 102249, PR China

^c National Institute of Metrology, Beijing 100013, PR China

ARTICLE INFO

Article history:

Received 11 June 2014

Received in revised form 6 September 2014

Accepted 11 October 2014

Available online 18 October 2014

Keywords:

SBA-15

Hydrodesulfurization

NiMo

Morphology.

ABSTRACT

Mesoporous SBA-15 materials with different morphologies were successfully synthesized through different methods by using pluronic P123 triblock copolymer (EO₂₀PO₇₀EO₂₀) and cosurfactant (CTAB) as structure-directing agent. Moreover, highly ordered mesoporous Al-SBA-15 with a Si/Al molar ratio of 10 has been prepared with three different Al resources using post-synthesis methods. The characterization results of X-ray fluorescence spectroscopy, X-ray power diffraction, N₂ adsorption–desorption and ²⁷Al nuclear magnetic resonance spectroscopy revealed that the chemical grafting of aluminum chloride on the surface of SBA-15 was the best post-synthesis route for the preparation of Al-SBA-15 with different morphologies. The corresponding Al-SBA-15-supported NiMo hydrodesulfurization (HDS) catalysts with different morphologies were prepared and evaluated using DBT as a probe reactant. The sphere NiMo/AS-SP catalyst has higher dispersion degree of MoS₂ slabs and more acid sites than other catalysts. The catalytic results showed that the morphologies and mesochannels of SBA-15 played an important role in the catalytic performance of DBT HDS over NiMo catalysts, especially in the diffusivity of DBT molecules in the catalysts, while they have little effect on the selectivity of DBT HDS. The kinetics investigations confirmed that the activity of DBT HDS over these catalysts followed the order: long-rod catalyst (NiMo/AS-LR) < hexagonal prism catalyst (NiMo/AS-HP) < short-rod catalyst (NiMo/AS-SR) < sphere catalyst (NiMo/AS-SP). The high activity of the last one was attributed to the superior diffusion of the supports and the better dispersion of the active components.

© 2014 Elsevier B.V. All rights reserved.

1. Introduction

The sulfur compounds of the exhaust emissions from gasoline and diesel fuels combustion processes are the major components of air pollutants, which are very harmful to human health and the environment, and therefore, sulfur contents in transportation fuels should be limited to near zero in the stringent fuel specification [1,2]. Various methods to remove the S in oil distillates have been proposed in many developed countries, such as hydrogenation, adsorption, biological desulfurization, etc. Among these technologies, the most effective process in large-scale industrial production is the catalytic hydrotreating [3]. However, the traditional hydrodesulfurization technique has been

confronted a great challenge since the S limitation in the EU-V fuel specification was restricted lower than 10 ppm, meaning that the highly refractory molecules such as dibenzothiophene and 4,6-dimethyldibenzothiophene need to be desulfurized in the hydrotreating process [4,5]. In order to meet the demands of ultra-clean fuels, novel HDS catalysts with high selectivity and activity have been paid more attention. Compared with the conventional HDS-support γ -Al₂O₃, hierarchical porous materials can not only offer space for dispersing the catalytic active species, but also provide acid sites for the HDS reactions. Recently, the synthesis of novel supports becomes the special issue of the design and development of hydrotreating catalysts.

Soni et al. [6] reported that KIT-6-supported Mo, CoMo, and NiMo catalysts exhibited higher activities for the conversion of thiophene than γ -Al₂O₃-supported catalysts. Zhang et al. [2] prepared a novel micro-mesoporous composite material Beta-KIT-6 (BK) and used as the catalyst support for hydrodesulfurization of dibenzothiophene. The result showed that NiMo/Beta-KIT-6

* Corresponding author. Tel./fax: +86 10 8973 1283.

E-mail addresses: duanaijun@cup.edu.cn, duanaijun@163.com (A. Duan), zhangxin@cup.edu.cn (X. Zhang).

exhibited a higher activity than the NiMo/ γ -Al₂O₃ catalyst due to the superior mass transfer ability of the cubic Ia3d mesoporous structure. Li et al. [7] prepared NiW/Al-SBA-15 catalyst and used in hydrodesulfurization. They found that it showed a higher hydrodesulfurization activity than the NiW/ γ -Al₂O₃ catalyst because of the perfect combination of the better dispersion and higher stacking of Ni-W-S phases on the support with the suitable distributions of B and L acid sites simultaneously. Mesoporous silica materials with high surface areas and well-ordered pore structures have potential applications in the catalytic conversion processes of large molecules because their large pore sizes can mitigate the diffusion barrier of the reactants and the products. Mesoporous SBA-15 [8,9] material synthesized using pluronic P123 triblock copolymer (EO₂₀PO₇₀EO₂₀) as SDA has relatively large pore and shows high hydrothermal stability due to its special configuration. Many researchers have employed SBA-15-type materials as the supports of hydrodesulfurization catalysts [10–13]. However, compared with the conventional microporous zeolites [14], SBA-15 has much weaker acidity and lower hydrothermal stability because of its neutral silicon frameworks. Thus, how to substantially improve the hydrothermal stability and the acidity of SBA-15 attracts more interests. Al-containing SBA-15 material prepared by partial replacement of silicon ions with aluminum ions can improve the hydrothermal and acidity of SBA-15 [15–18]. Luan et al. [19] reported that Al could not be constructed into the SBA-15 structure by direct incorporation method, because most of the Al sources can dissolve in the strong acidic media. Therefore, the post-synthetic method that can graft Al³⁺ into the SBA-15 surface seems to be an alternative choice to prepare Al-SBA-15.

Besides the acidity of SBA-15, the morphology, pore size, and pore structure of SBA-15 also have influence on the activity of catalytic reactions [7,20–22]. The shape and size of mesoporous SBA-15 particles are crucial factors for the reactant and the product molecules diffusing in the particle channels, where the subsequent undesirable reactions might take place [23]. And the morphology of SBA-15 also plays an important role in dispersion of active metal species in the support mesopores which will improve the performance of the catalysts. Katiyar et al. [24] reported that the spherical SBA-15 particles had a higher saturation capacity than the fibrous particles on the adsorption of proteins. Chen [25] also synthesized a functionalized mesoporous SBA-15 with platelet morphology and short mesochannels. And the platelet SBA-15 materials were superior to the conventional SBA-15 materials with rod or fiber morphologies in facilitating the molecular diffusion and reducing the pore blockage when they were used in the adsorption or reactions of bulky molecules. Till now, many efforts have been devoted to the synthesis of mesoporous materials with uniform size and well-defined morphology. Mesoporous SBA-15 materials in the forms of rod, sphere, fiber, platelet, gyroid, discoid, sausage, and doughnut shapes have been obtained through various synthetic strategies [26–31]. It has been well documented that the catalytic properties are related to the morphology and composition of material [5,32,33]. However, no detailed studies have been made to investigate the effect of morphology on the HDS activity over SBA-15-supported catalysts.

In this research, a series of SBA-15 materials with different morphologies were successfully synthesized using pluronic P123 triblock copolymer and cosurfactant (CTAB) as structure-directing agent. And three different post-synthesis routes to incorporate Al into SBA-15 were used to prepare Al-SBA-15 materials. The as-synthesized Al-SBA-15-supported NiMo catalysts with different morphologies were prepared through a two-step incipient-wetness impregnation method, and the corresponding HDS performances were evaluated using dibenzothiophene as probe molecules, while the conventional NiMo/ γ -Al₂O₃ catalyst was taken as the reference. The effects of different

morphologies of SBA-15 on the catalytic performances of DBT HDS were systematically investigated at different temperatures and weight times. Furthermore, the physicochemical properties of the supports and catalysts were characterized by various characterization techniques. The HDS results of DBT over these catalysts follow the activity order: long-rod catalyst (NiMo/AS-LR) < hexagonal prism catalyst (NiMo/AS-HP) < short-rod catalyst (NiMo/AS-SR) < sphere catalyst (NiMo/AS-SP). A possible reaction network of DBT HDS over NiMo supported on Al-SBA-15 catalysts with different morphologies was also proposed.

2. Experiment

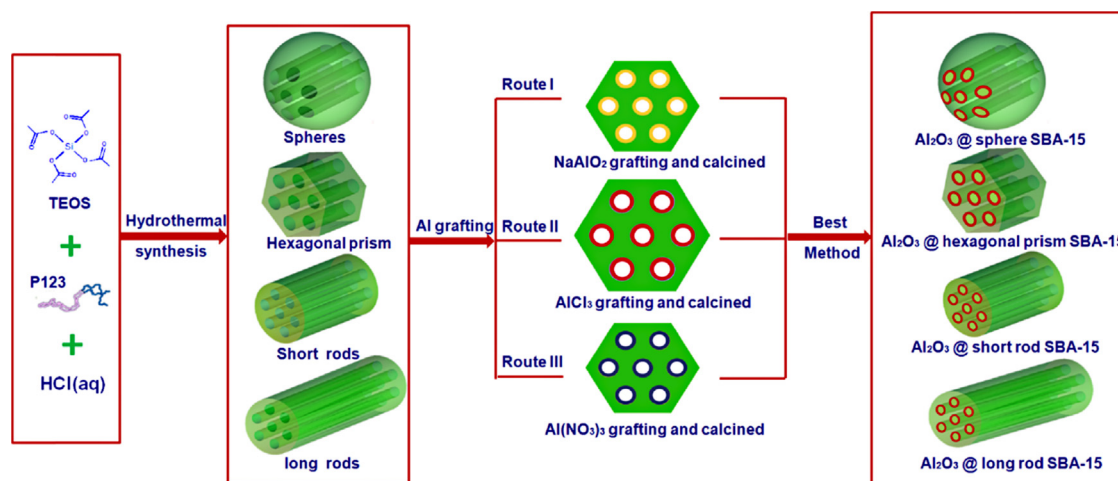
2.1. Synthesis of the supports

Mesoporous SBA-15 silicas with different morphologies were synthesized using Pluronic P123, cetyltrimethylammonium bromide (CTAB) as the structure-directing agent, and tetraethyl orthosilicate (TEOS) as the silicate source under acidic conditions. All commercial chemicals were used without further purifications. Three different morphologies of SBA-15, hexagonal prisms, short rods, and long rods were synthesized under different temperatures with the same compositions of the original reaction mixtures. In a typical synthesis, 2 g of P123 was dissolved in 65 g of HCl (2 mol/L). The temperatures of P123 solution for hexagonal prisms, short rods, and long-rod SBA-15 were controlled at 35, 45 and 55 °C respectively. Then, 4.28 g of TEOS was added in P123 solution under confined stirring rate for 3 min and further maintained at static condition for 24 h. The gel solutions were transferred into a Teflon bottle and heated at 100 °C for 24 h without stirring. After cooling to the room temperature, SBA-15 with three different morphologies was recovered by filtering and drying at room temperature in air. Then, all samples were calcined at 550 °C for 6 h to remove the copolymer template. A sphere mesoporous SBA-15 was synthesized using P123 and CTAB as cosurfactant according to the above procedure, except that the hydrolysis temperature of TEOS was controlled at 40 °C. A typical reaction composition was 2.0 g P123:0.4 g CTAB:45.0 g HCl (2 M):15.0 g H₂O:5.8 g TEOS. The SBA-15 with spheres, hexagonal prisms, short rods, and long rods morphologies were denoted as SP, HP, SR, and LR, respectively.

These mesoporous silica SBA-15 were used as precursor materials to produce Al-containing SBA-15 with a Si/Al molar ratio of 10 via the post-synthetic alumination method according to the literature [15]. The scheme for the preparation procedure of Al-SBA-15 composite with different morphologies was shown in Scheme 1. We used the short-rod SBA-15 (SR SBA-15) as the parent material to evaluate the best method to incorporate Al, via the post-synthesis routes using different kinds of Al sources, involving NaAlO₂, Al(NO₃)₃, and AlCl₃. Routes I–III represent the different ways to incorporate Al by using three different Al precursors. The typical procedure is that 1 g of SBA-15 was dispersed with solvent containing the required amount of Al precursor. This mixture was kept with magnetic stirring at room temperature for 12 h. The solid material was then filtered, washed vigorously with distilled water, and dried at 80 °C in air. The obtained aluminum-containing materials were calcined in static air at 550 °C for 6 h. The Al precursors of Routes I–III were NaAlO₂, AlCl₃, and Al(NO₃)₃, respectively. And the solvents of Routes I–III were water, dry ethanol, and water, respectively. The supports of Al-SBA-15 modified with NaAlO₂, AlCl₃, and Al(NO₃)₃ were denoted as AS-N, AS-C, and AS-O, respectively.

2.2. Preparation of the catalysts

The different morphology mesoporous SBA-15 doped with Al by using AlCl₃ as Al precursor were used as the support of the



Scheme 1. Preparation of the Al-SBA-15 mesoporous materials with different morphologies.

catalysts. The supported NiMo catalysts were prepared by two-step incipient-wetness impregnation of ammonium heptamolybdate and nickel nitrate, with Mo impregnated in the first and Ni in the second. During the impregnation of Mo, the metal precursors were dissolved with a 0.5 M oxalic acid [34]. After each impregnation step, the samples were dried at 100 °C for 24 h and calcined at 550 °C for 6 h in air. The NiMo catalyst supported on γ -Al₂O₃ was also prepared as a reference catalyst. The nominal composition of the catalysts was 11 wt% of MoO₃ and 3.5 wt% of NiO. The obtained samples were crushed into 0.3–0.5 mm particles. The resulting catalysts were denoted as NiMo/AS-SP (NiMo/spheres Al-SBA-15), NiMo/AS-HP (NiMo/hexagonal prisms Al-SBA-15), NiMo/AS-SR (NiMo/short-rod Al-SBA-15), NiMo/AS-LR (NiMo/long-rod Al-SBA-15), and NiMo/ γ -Al₂O₃.

2.3. Characterizations

The surface morphology of the supports and catalysts was observed by field emission scanning electron microscopy (FESEM) on a Quanta 200F instruments using accelerating voltages of 20 kV. The silica-based samples were coated with gold before the SEM measurement. TEM images were taken from thin edges of particles supported on a porous carbon grid using a JEOL JEM 2100 electron microscope operated at 120 kV.

Surface areas and pore size distributions of the samples were measured by nitrogen isotherms using a Micromeritics ASAP 2010 system at liquid nitrogen temperature. The samples to be measured were first degassed in the preparation station at 300 °C under vacuum and then switched to the analysis station for adsorption–desorption at liquid nitrogen temperature. The pore size distributions of the samples were calculated using the Barrett–Joyner–Halenda (BJH) method. The surface areas were calculated using the Brunauer–Emmett–Teller (BET) model. The total volumes of micro- and mesopores were calculated from the amounts of nitrogen adsorbed at $P/P_0 = 0.98$, assuming that adsorption on the external surface was negligible compared to the adsorption in pores.

The low-angle ($2\theta = 0.5$ – 5.0°) X-ray diffraction patterns of the supports and catalysts were measured on a Bruker D8 Advance Powder diffractometer using Cu K α radiation and the scattering slits of 0.05°. The wide-angle ($2\theta = 5.0$ – 80.0°) XRD patterns were performed on a powder X-ray diffractometer (Shimadzu XRD 6000) using Cu K α ($\lambda = 0.15406$ nm) radiation and with a scanning rate of 4°/min. The Si/Al molar ratio of the supports was determined by X-ray fluorescence spectroscopy (XRF) conducted on a Rigaku

ZSX-100e instrument. The Raman spectra were obtained using a Renishaw Raman InVia Microscope (Spectra-Physics model 163), operated at the argon ion laser with a wavelength of 514 nm. The laser spot size was approximately 1–2 μ m with a power of 3.6 mW. The UV–Vis diffuse reflectance spectroscopy (UV–Vis DRS) experiments were recorded on a UV–Vis spectrophotometer (Hitachi U-4100) with the integration sphere diffuse reflectance attachment. The powder catalysts were loaded in a transparent quartz cell and characterized in the region of 200–800 nm at room temperature.

The nature of the acid sites over the catalysts was determined by pyridine-FTIR on self-supported wafers in an in situ FTIR cell. The samples were dehydrated at 400 °C for 2 h under a vacuum of 1.33×10^{-3} Pa, followed by adsorption of purified pyridine vapor at room temperature for 20 min. The system was then degassed and evacuated at different temperatures (200 and 350 °C) for 2 h, and the IR spectra were recorded. ²⁷Al NMR experiments of Al-SBA-15 materials obtained by different post-synthesis methods were carried out on a Bruker AVANCE III 600 spectrometer at a resonance frequency of 156.4 MHz using a 4 mm HX double-resonance MAS probe at a sample spinning rate of 15 kHz. The chemical shift of ²⁷Al was referenced to 1 M aqueous Al(NO₃)₃. ²⁷Al MAS NMR spectra were recorded by small-flip angle technique with a pulse length of 0.5 μ s ($<\pi/12$) and a 1 s recycle delay and 2400 scans.

2.4. Catalytic performance evaluation

The catalytic activities of the catalysts were evaluated using 0.5 wt% DBT in cyclohexane as a model compound. The reactions were carried out in a continuously flowing tubular fixed-bed inonel reactor (8 mm inner diameter and 400 mm in length) loaded with 0.5 g catalyst diluted with quartz particles to keep a constant total solid weight of 3.0 g. All catalysts were presulfided for 4 h with H₂ and 2 wt% CS₂ in cyclohexane at 360 °C and 4 MPa. After sulfidation, the HDS reactions were performed under the conditions of temperature 340 °C, total pressure 4.0 MPa, and H₂/hydrocarbon 200 mL/mL. Reactant liquid was fed to the reactor by a SZB-2 double-piston pump. Weight time was defined as $\tau = \omega_{\text{cat}}/\eta_{\text{feed}}$, where ω_{cat} denotes the catalyst weight and η_{feed} represents the total molar number of feed-stock flowing into the reactor [35]. The DBT HDS reaction of the catalysts was conducted at different weight times (τ) by varying the flow rates of the gas and the liquid reactants. In addition, the reaction was also carried out at different temperatures, such as 300, 320, 340, 360, and 380 °C, to determine the

influences of temperature on the HDS performance of DBT. During the reaction, the weight time was confined at $2.8 \text{ g min mol}^{-1}$. After presulfidation, the steady state could be reached after 2 h on stream at each temperature. Under the steady operation conditions, the sulfur contents in the products keep constant, thus we could collect the liquid products to analyze the sulfur contents and the product distribution.

The sulfur contents of the reactants and the products were tested by a RPP-2000SN sulfur and nitrogen analyzer (Taizhou Central Analytical Instruments Co. Ltd., P.R. China). To corroborate the product compositions, the product mixtures were analyzed in a Thermo-Finnigan Trace DSQ GC-MS coupled with a HP-5MS column ($60 \text{ m} \times 0.25 \text{ mm} \times 0.25 \mu\text{m}$).

2.5. Kinetic analysis

In reference [36], the pseudo-first-order kinetics fit well with the experimental results of DBT HDS. Thus, in this work, the catalyst activity was assumed to follow a pseudo-first-order kinetics according to the following equation:

$$k_{\text{HDS}} = \frac{F}{m} \ln \left(\frac{1}{1-\eta} \right) \quad (1)$$

where k_{HDS} is the rate constant of HDS in $\text{mol g}^{-1} \text{ s}^{-1}$, F is the feeding rate of the reactant in mol s^{-1} , m is the catalyst mass in g, and η is the total conversion of DBT. The experimental data from the HDS reactions of DBT was used to calculate the reaction rate constants k_{HDS} ; only the DBT at conversions below 30% was considered. In addition, the HDS rates of different NiMo-supported catalysts were also obtained in terms of turn-over frequency (TOF). TOF was calculated as a parameter to estimate the DBT molecules reacted per second and per Mo atom located on the edges of MoS_2 crystallite [37]. The number of Mo atoms located on the edge surface was estimated using the total amount of Mo and the fraction of Mo atoms on the edge surface of MoS_2 particles, which denoted as f_{Mo} . The f_{Mo} value was achieved from Eq. (2), assuming that the MoS_2 crystals were perfect hexagons [38,39]. Here in Eqs. (2) and (3), n_i is the number of Mo atoms along one edge of MoS_2 slabs determined from the length L (HRTEM), and t is the total number of layers determined from 20 micrographs including about 300 slabs.

$$f_{\text{Mo}} = \frac{\sum_{i=1}^t (6n_i - 6)}{\sum_{i=1}^t (3n_i^2 - 3n_i + 1)} \quad (2)$$

$$n_i = \frac{L}{6.4} + 0.5 \quad (3)$$

In addition, the well-known Arrhenius and Eyring equations were applied to calculate the activation parameters and the correlation graphs of $\ln k_{\text{HDS}}$ vs $1/T$, and $\ln(k/T)$ vs $1/T$ were constructed [40,41].

$$\ln k_{\text{HDS}} = \ln A - \left(\frac{E_a}{RT} \right) \quad (4)$$

$$\ln \left(\frac{k_{\text{HDS}}}{T} \right) = \ln \left(\frac{k_B}{h} \right) + \left(\frac{\Delta S}{R} \right) - \left(\frac{\Delta H}{R} \right) \left(\frac{1}{T} \right) \quad (5)$$

Here in Eqs. (4) and (5), k_{HDS} is the rate constant of the reactions ($\text{mol g}^{-1} \text{ s}^{-1}$), T is absolute temperature (K), k_B is Boltzmann's constant ($1.381 \times 10^{-23} \text{ J K}^{-1}$), h is Planck's constant ($6.626 \times 10^{-34} \text{ J s}$), E_a is the activation energy (kJ mol^{-1}), ΔH is the activation enthalpy (kJ mol^{-1}), ΔS is the activation entropy ($\text{J mol}^{-1} \text{ K}^{-1}$), and R is the ideal gas constant ($8.314 \text{ J K}^{-1} \text{ mol}^{-1}$).

3. Results

3.1. Characterization of short-rod SBA-15 modified with Al by using different aluminum sources

The pure SBA-15 material has much weaker acidity and lower hydrothermal stability because of its neutral silicon frameworks. Thus, it is necessary to improve the hydrothermal stability and acidity of SBA-15 by partial replacement of silicon ions with aluminum ions. Klimova et al. [42] reported that NiMo catalysts supported on Al-containing SBA-15 materials with a Si/Al molar ratio between 30 and 10 show high activity in HDS of 4,6-dimethyldibenzothiophene. Suresh et al. [43] also prepared Mo-Ni/Al-SBA-15 catalysts with a Si/Al molar ratio of 10 and showed an impressive catalytic performance for methylcyclohexylamine conversion to hydrocarbons. Therefore, Al-containing SBA-15 with a Si/Al molar ratio of 10 (theoretical content) was used in this study for DBT HDS. In addition, Luan et al. [19] reported that Al was difficult to be constructed into the SBA-15 structure by direct incorporation method, because most of Al species can dissolve in the strong acidic media. And the post-synthetic method which can graft Al^{3+} into the SBA-15 surface was an alternative choice to prepare Al-SBA-15.

3.1.1. XRD of Al-SBA-15 with SR morphology

The low-angle XRD patterns of pure silicon SBA-15 with different morphologies are shown in Fig. 1A. The pure silicon SBA-15 with different morphologies exhibit three well-resolved diffraction peaks, indexed as (100), (110) and (200) reflections respectively, which imply that they all possess highly ordered hexagonal ($p6mm$) symmetry and well-ordered mesoporous structure. The unit cell parameter a_0 of the four samples are different with each other, which may be due to the different synthesis temperatures and the additions of cosurfactant [8].

Compared to the pure silica SBA-15, the low-angle XRD patterns of the Al-SBA-15 materials modified with different alumina species are shown in Fig. 1B, which exhibit a shift in the reflection peaks to the wider angle. This shift corresponds to the decreased length of the unit cell a_0 , which can be calculated from the formula $a_0 = d_{100} \times 2/3^{1/2}$ [8]. All the samples exhibit three well-resolved diffraction peaks, indexed as (100), (110) and (200) reflections, respectively, which indicates that Al-SBA-15 modified with alumina also have highly ordered hexagonal ($p6mm$) symmetry. In Table 1, the sample AS-N shows the largest decreased length of the unit cell a_0 , falling from 11.40 to 10.74 nm, then followed by AS-O (11.40 to 11.09 nm), and AS-C (11.40 to 11.19 nm), respectively.

3.1.2. SEM of Al-SBA-15 with SR morphology

The SEM images of Al-SBA-15 modified with different alumina sources are displayed in Fig. S1. SEM images reveal few differences between the pure silica SBA-15 and the aluminum-containing Al-SBA-15. All the samples show the short-rod morphology with a relatively uniform length of $350 \times 1000 \text{ nm}$. It indicates that the post-synthesis alumination methods have no effect on the final morphology of Al-SBA-15.

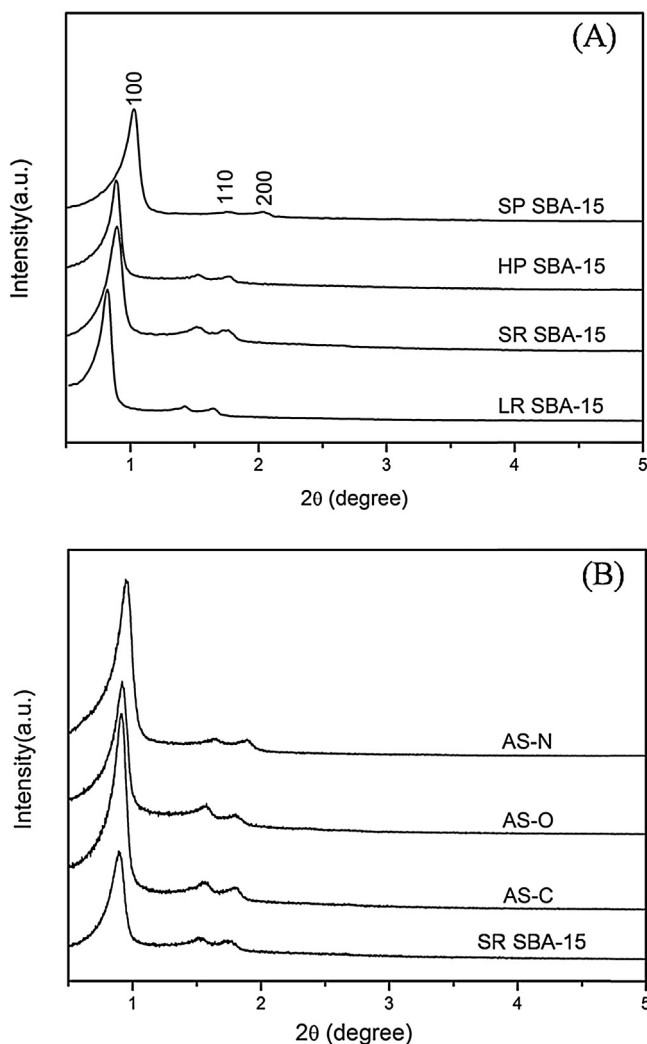
3.1.3. BET of Al-SBA-15 with SR morphology

Fig. 2 shows the N_2 adsorption-desorption isotherms and pore size distribution curves of short-rod SBA-15 and short-rod Al-SBA-15 modified with different alumina sources. The pore size distributions of SBA-15, AS-N, AS-O, and AS-C, calculated from the adsorption branch of the isotherms, show a narrow distribution of mesopores. The materials of SBA-15, AS-N, AS-O, and AS-C exhibit similar type IV isotherms with H1-type hysteresis loops, which are the typical behaviors of ordered mesoporous structure. The Al-grafted SBA-15 materials induced a slight reduction in the N_2

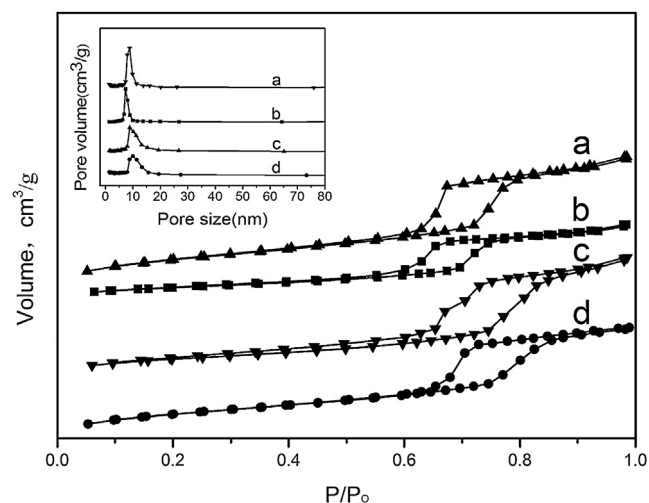
Table 1

Textural and structural characteristics of SBA-15 and Al-SBA-15 modified with different alumina sources.

Samples	S_{BET}^a (m^2/g)	V_t^b (cm^3/g)	V_{mes}^c (cm^3/g)	V_{mic}^d (cm^3/g)	$V_{\text{mic}}/V_{\text{mes}}$	a_0^e (nm)	d_{BJH}^f (nm)	$\text{Al}_{\text{tet}}/(\text{Al}_{\text{tet}} + \text{Al}_{\text{oct}})^g$	Si/Al^h
SBA-15	776	1.07	1.04	0.13	0.12	11.4	8.2	–	–
AS-N	315	0.59	0.58	0	0	10.7	6.5	1.0	7.6
AS-O	424	0.91	0.90	0.02	0.02	11.0	7.8	0.7	23.6
AS-C	638	0.90	0.86	0.11	0.13	11.2	7.6	0.6	16.7

^a Calculated by the BET method.^b The total pore volume was obtained at a relative pressure of 0.98.^c Calculated using the BJH method.^d Calculated using the t -plot method.^e XRD unit cell parameter (a_0) was estimated from $a_0 = d_{100} \times 2/3^{1/2}$.^f Mesopore diameter calculated using the BJH method.^g Calculated from ^{27}Al MAS NMR spectra assuming that the relative content of aluminum is proportional to the intensity of the ^{27}Al MAS NMR lines.^h Determined by XRF.**Fig. 1.** XRD patterns of the as-synthesized materials. (A) Pure SBA-15 silica with different morphologies in the small-angle domain; (B) short-rod SBA-15 modified with different alumina sources in the small-angle domain.

adsorption capacity. Furthermore, compared with AS-O and AS-C, the isotherm of AS-N modified with NaAlO_2 only shows a weak capillary condensation effect, which may be derived from the collapse of the porous structure [19]. A vertical shift in the desorption curve is observed in the range of $P/P_0 = 0.65$ – 0.70 for the AS-O sample, which may be resulted from the partially plugged mesopores [44]. Textural and structural characteristics of SBA-15 and Al-SBA-15 modified with different alumina sources are summarized in Table 1. It is found that the surface area, pore volume, and pore size

**Fig. 2.** N_2 adsorption-desorption isotherms and pore size distribution curves of short-rod SBA-15 and short-rod Al-SBA-15 modified with different alumina sources. (a) Short-rod SBA-15, (b) AS-N, (c) AS-O, (d) AS-C.

of SBA-15 incorporated with aluminum through post-synthetic procedure decrease apparently. Compared with the pure silica SBA-15, the sample of AS-N shows the greatest decrease in the surface area, falling from 776 to $315 \text{ m}^2/\text{g}$, followed by AS-O (776 to $424 \text{ m}^2/\text{g}$) and AS-C (776 to $638 \text{ m}^2/\text{g}$), respectively. The pore volume of the sample AS-C is larger than those of AS-N and AS-O, which were synthesized by NaAlO_2 and $\text{Al}(\text{NO}_3)_3$, respectively. In addition, the mean pore diameters of the short-rod SBA-15, AS-N, AS-O, and AS-C are 8.0 , 6.5 , 7.8 , and 7.6 nm respectively. The Si/Al values of different samples calculated from XRF reveal that the AS-N sample has a lower Si/Al ratio than the expected value (10), indicating that almost all of the Al species added in the reaction mixture have been grafted into the AS-N sample. Furthermore, the measured Si/Al ratio of AS-C is slightly higher than 10 , while the value of AS-C increases to 23.6 . These results accorded well with the XRD results of the corresponding materials.

3.1.4. ^{27}Al MAS NMR of Al-SBA-15 with SR morphology

^{27}Al MAS NMR spectroscopy was performed to analyze the way by which aluminum interacted with the SBA-15 framework. The ^{27}Al MAS NMR spectra (Fig. 3) of Al-SBA-15 show that three types of peaks can be observed in AS-O and AS-C. Three signals with maxima centered at 0 , 30 , and 54 ppm are assigned to the octahedral, pentahedral, and tetrahedral aluminum atoms, respectively [45]. The percentage of each coordinated aluminum species can be calculated from the relative intensities of the corresponding line in the ^{27}Al MAS NMR spectra. The distributions of octahedral, pentahedral, and tetrahedral Al species in AS-O and AS-C can be evaluated

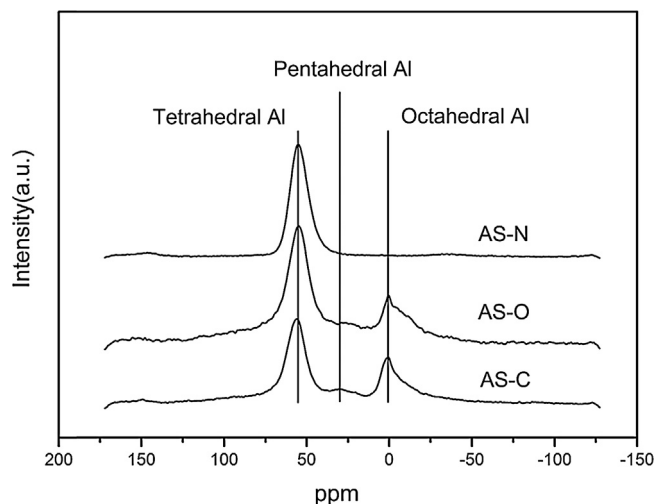


Fig. 3. ^{27}Al MAS NMR spectra of short-rod Al-SBA-15 modified with different alumina sources.

in ratios of 10/1/20 and 11/1/19, respectively, which are different from the conventional $\gamma\text{-Al}_2\text{O}_3$ support. This indicates that about 65 and 61% of aluminum atoms are incorporated into the silica framework of AS-O and AS-C supports, respectively. In contrast, the ^{27}Al MAS NMR spectra of AS-N, prepared by chemical grafting method using sodium aluminate as alumina source, shows only one peak at 54 ppm, indicating that all the aluminum species have been incorporated into the siliceous framework of short-rod SBA-15. It seems that the proportion of framework and extra-framework Al species in Al-SBA-15 are determined by aluminum source during the post-synthetic Al incorporation procedure.

Among these three methods, alumination by reacting the short-rod SBA-15 with the solution of alumina chloride can maintain the surface area and porous structure of the SBA-15, while the method using aluminum nitrate or sodium aluminate as alumina sources causes some structure disorder. According to the above results, chemical grafting of aluminum chloride on the surface of SBA-15 is the best post-synthesis method for the preparation of Al-SBA-15 with different morphologies.

3.2. Characterization of Al-SBA-15 with different morphologies and the corresponding NiMo catalysts

3.2.1. XRD of the oxide NiMo catalysts

Fig. 4A and B shows the low-angle and wide-angle XRD patterns of NiMo oxide catalysts with different morphologies, respectively. It can be clearly found that the three reflection characteristics of the SBA-15 hexagonal structure still present, indicating that the mesoporous structures are preserved after the supports loaded with Ni and Mo active metal components. The wide-angle XRD patterns of NiMo supported on Al-SBA-15 with different morphologies reveal that there are no characteristic peaks attributed to $\gamma\text{-Al}_2\text{O}_3$, indicating that the extra-framework aluminum is homogeneously distributed on the outer surface and in the mesopores of Al-SBA-15 with different morphologies. In addition, Fig. 4B shows a broad peak existing at $2\theta = 20\text{--}30^\circ$ for all the catalysts except for NiMo/ $\gamma\text{-Al}_2\text{O}_3$, which corresponds to the amorphous silica of SBA-15 material. The wide-angle XRD patterns of NiMo/ $\gamma\text{-Al}_2\text{O}_3$ shows four characteristic peaks at $2\theta = 36.8^\circ$, 39.3° , 46.2° , and 66.7° , which are attributed to $\gamma\text{-Al}_2\text{O}_3$ [46]. The XRD patterns of all the catalysts demonstrate that MoO_3 is well dispersed on the support surfaces since no bulk MoO_3 is detected in the range from 12° to 35° .

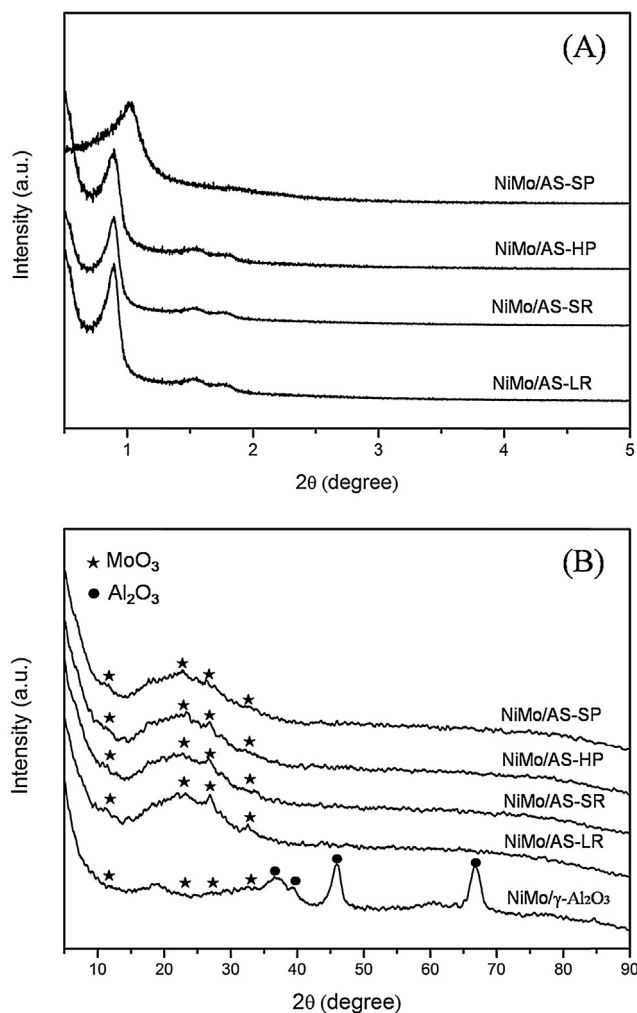


Fig. 4. XRD patterns of the catalysts with different morphologies. (A) The corresponding supported NiMo catalysts in the small-angle domain; (B) the corresponding supported NiMo catalysts in the wide-angle domain.

3.2.2. SEM of the supports and the oxide NiMo catalysts

The morphology of all the supports and catalysts was investigated by means of field emission scanning electron microscope (SEM). Fig. 5A1–D1 shows the changes in particle diameter and morphology of SBA-15 material due to different synthesis temperatures and structure-directing agents. With increasing initial reaction temperature, the particle size decreases significantly. According to the experimental results, as the temperature increases, the precipitation time decreases significantly. The higher initial temperature may accelerate the rate of hydrolysis and condensation of silica precursors, which favors the growth of SBA-15 along the length of the rods and decreases the widths of SBA-15. This phenomenon may be correlated to the local curvature energy that is present at the interface of amphiphilic block copolymer species and the inorganic silica. The mesoporous SBA-15 material can be formed in sphere particles state using the cationic surfactant CTAB as a cosurfactant, which suggests that the addition of cosurfactant can lower the local curvature energy and favor the formation of sphere SBA-15.

Fig. 5 also shows the SEM images of Al-SBA-15 and NiMo/Al-SBA-15 with different morphologies. All samples are highly monodispersed particles with respect to their characteristic shapes. Fig. 5A1–A3 shows the sphere types of SBA-15, AS-SP, and NiMo/AS-SP materials composed of spherical particles with heterogeneous diameter distributions. The morphology of AS-HP (Fig. 5B2) and

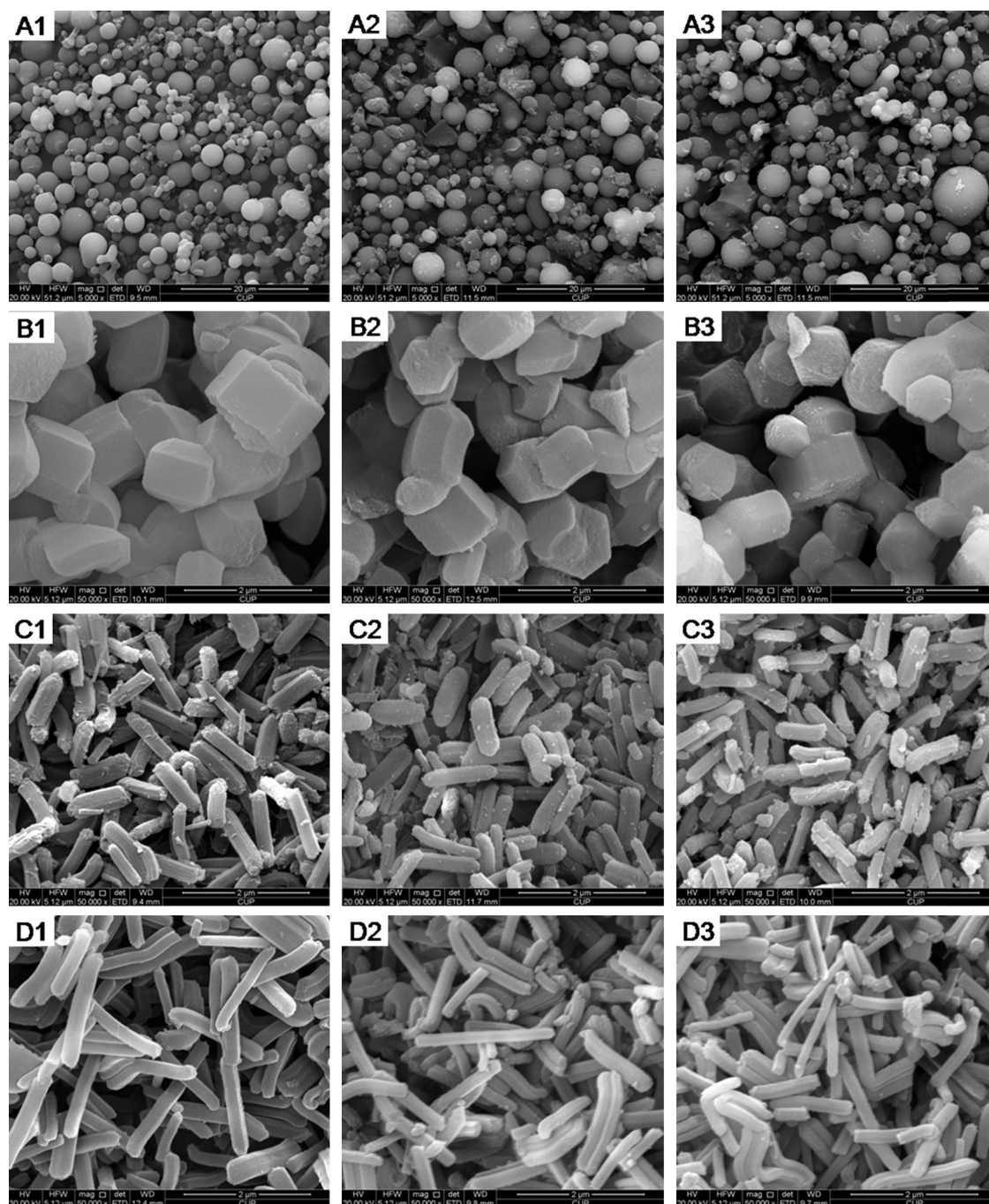


Fig. 5. SEM images of the as-synthesized SBA-15 with spheres (A), hexagonal prisms (B), short rods (C) and long rods (D) morphologies, respectively; (1), (2) and (3) represent the corresponding SBA-15, Al-SBA-15 and NiMo/Al-SBA-15.

NiMo/AS-HP (Fig. 5B3) keeps the same hexagonal prisms with the dimension in 900×1000 nm. The widths and lengths of short-rod SBA-15 (Fig. 5C1), AS-SR (Fig. 5C2), and NiMo/AS-SR (Fig. 5C3) are ~ 350 and ~ 1000 nm, respectively, while the widths and lengths of long-rod SBA-15 (Fig. 5D1), AS-LR (Fig. 5D2), and NiMo/AS-LR (Fig. 5D3) are ~ 250 and ~ 1500 nm, respectively. This indicates that the morphology of SBA-15 has no significant change after the incorporations of aluminum or NiMo active metal components.

3.2.3. TEM of the supports

Fig. 6 shows the TEM images of pure silica SBA-15 materials with different morphologies. All of these SBA-15 with different morphologies show well-ordered hexagonal arrays of mesopores and

confirm its 2D $p6mm$ hexagonal structure, which is consistent with the previous XRD results [8]. TEM images verify that the mesochannels of SBA-15 with hexagonal prism and rod morphologies run along the length direction of the particles. The mesochannels of sphere SBA-15 grow along with the diameter of the sphere. Their large pores (5.5–8.5 nm) are clearly visible in the TEM images, which is consistent with the N_2 adsorption results. The morphologies and sizes of SBA-15 observed from TEM are in agreement with the observation by SEM images. These perfect mesoporous structures and high accessibilities provide the ideal reaction space for the hydrosulfurization of dibenzothiophene which have relatively large kinetic diameters and steric hindrance. Therefore, the number of contact points between dibenzothiophene and the catalysts will

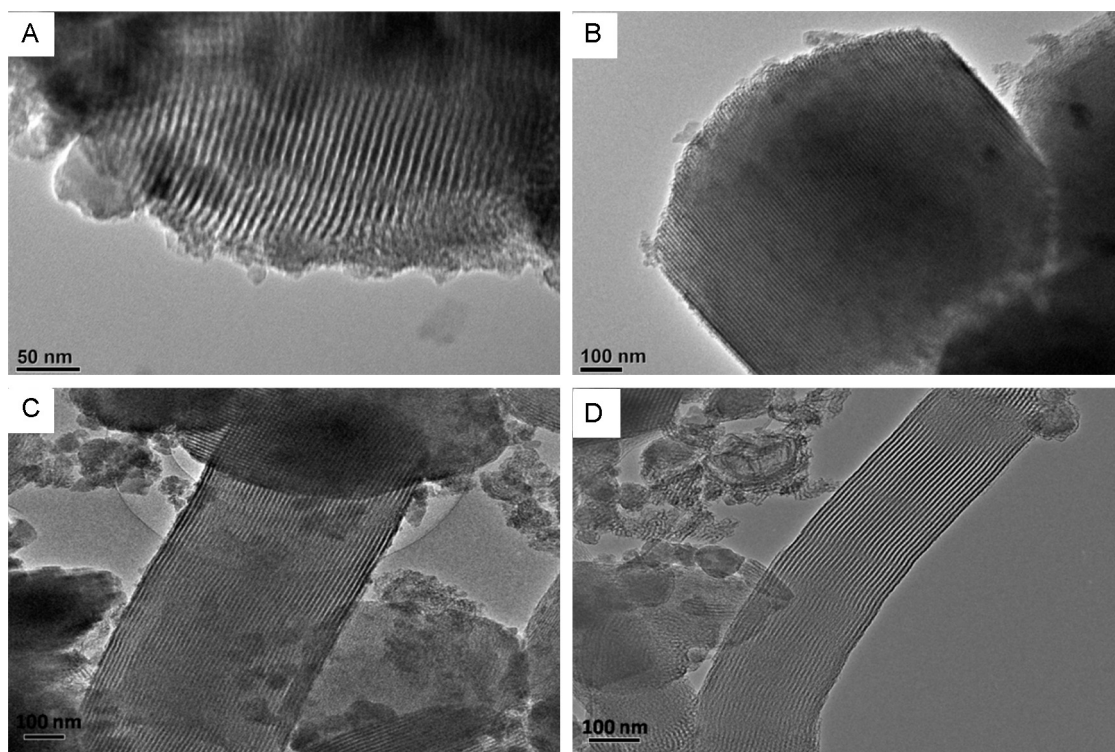


Fig. 6. TEM images of the SBA-15 samples with different morphologies. (A) Spheres SBA-15, (B) hexagonal prisms SBA-15, (C) short-rod SBA-15, (D) long-rod SBA-15.

be increased dramatically. In addition, all of external surface over the sphere SBA-15 mesoporous material distributes with mesopore cavities, and the internal surface has high connectivity, which can be clearly found from Fig. S2. Thus, the active component species have an better dispersion on the sphere support mesoporous during the preparation of the catalysts. In comparison to the spheres SBA-15, the mesochannel orifices of the hexagonal prisms and rods SBA-15 only exist at both ends, indicating that the metal precursors are not easy to access the internal surface of mesochannels, then the diffusivities of the active components and reactant DBT in the hexagonal prisms and rods SBA-15 catalysts are inferior to the spheres SBA-15.

3.2.4. BET of the supports and the oxide NiMo catalysts

The N_2 adsorption–desorption isotherms and the pore size distribution curves of the pure silicon SBA-15 with different morphologies are shown in Fig. S3. The materials of spheres SBA-15, hexagonal prism SBA-15, short-rod SBA-15, and long-rod SBA-15 all show the similar type IV isotherms with H1-type hysteresis loop and narrow mesoporous distributions, which are the typical behaviors of the ordered mesoporous structure [47]. The isotherm exhibits a sharp inflection in the P/P_0 range from 0.50 to 0.85, which is a characteristic of capillary condensation within uniform mesostructure. In addition, N_2 adsorption–desorption isotherms and pore size distribution curves (Fig. S3B) of NiMo supported on Al-SBA-15 catalysts with different morphologies also show the type-IV isotherms with H1-type hysteresis loops and a relatively narrower pore size distribution. In comparison, NiMo/ γ - Al_2O_3 catalyst shows a H4-type hysteresis loop and a broad pore diameter distribution, which can be attributed to the inter-particle space. Therefore, there is little change in the shape of the hysteresis loops and the pore diameter distribution between different supports and their corresponding catalysts.

The textural properties of the supports and the supported NiMo catalysts are summarized in Table 2. The pure silicon SBA-15 with different morphologies has different surface areas in the

following the order of HP ($733\text{ m}^2/\text{g}$) < SR ($776\text{ m}^2/\text{g}$) < LR ($797\text{ m}^2/\text{g}$) < SP ($890\text{ m}^2/\text{g}$). The pore diameters of the supports follow the order of SP (5.8 nm) < HP (7.4 nm) < SR (8.2 nm) < LR (8.6 nm). These data indicate that the high synthesis temperature can increase the surface areas and the pore diameters of SBA-15. The surface areas and pore volumes of the catalysts significantly decrease after loaded with the active metals of Ni and Mo. The surface areas of NiMo/AS-SP, NiMo/AS-HP, NiMo/AS-SR, NiMo/AS-LR, and NiMo/ γ - Al_2O_3 decrease by 44, 45, 47, 51, and 25%, respectively, indicating that the surface areas of the SiO_2 -based supported catalysts decrease more than that of Al_2O_3 -supported catalysts, which is consistent with the previous work of Shimada et al [48]. In addition, the average pore diameters of NiMo/AS-SP, NiMo/AS-HP, NiMo/AS-SR, and NiMo/AS-LR are 5.5, 6.9, 8.0, and 8.5 nm, respectively. The decreased surface areas and pore diameters of the catalysts derived from the incorporation of Ni and Mo into the mesopores of the supports.

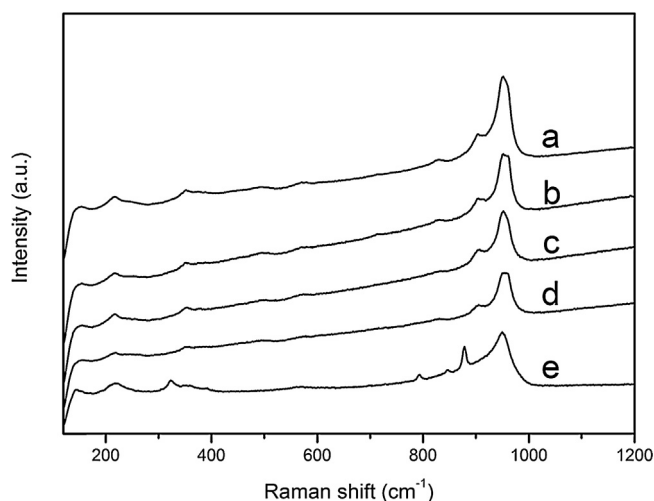
3.2.5. Raman spectroscopy of the oxide NiMo catalysts

Raman spectra is obviously sensitive to the crystalline symmetry and reflects the nature of the oxide phases presented on the catalyst [49]. The Raman spectra of the NiMo catalysts with different supports are displayed in Fig. 7. All the catalysts exhibit a typical band at 220 cm^{-1} ascribed to Mo–O–Mo deformation. The Mo–O–Mo linkages can be attributed to the presence of polymolybdates in the catalysts. The bands at ~ 955 , ~ 908 , and $\sim 826\text{ cm}^{-1}$ can be associated with $NiMoO_4$ precursor phase [11,20]. The broad band in the region of 890 – 1000 cm^{-1} , which overlaps with the Mo=O stretching vibrations at $\sim 990\text{ cm}^{-1}$, can be assigned to the Mo species interacting with the support [50]. The broad feature of this peak indicates the existence of a well-dispersed amorphous phase of MoO_x existing on the support surface, which is consistent with the XRD analysis. Compared to NiMo/Al-SBA-15 catalysts, the band in the range of 890 – 1000 cm^{-1} presented in the γ - Al_2O_3 -supported catalyst is relatively broader, demonstrating that the MoO_x phase is more surface interacting and amorphous in γ - Al_2O_3 .

Table 2

Textural properties of the supports and NiMo catalysts.

Sample	Morphology	Dimensions (ca. nm)	S_{BET}^a (m ² /g)	V_t^b (cm ³ /g)	V_{mes}^c (cm ³ /g)	V_{mic}^d (cm ³ /g)	$V_{\text{mic}}/V_{\text{mes}}$	d_{BJH}^e (nm)
SP	Spheres	3600 × 3600	890	0.98	0.96	0.02	0.02	5.8
HP	Hexagonal prisms	900 × 1000	733	0.91	0.81	0.05	0.06	7.4
SR	Short rods	350 × 1000	776	1.07	1.04	0.13	0.13	8.2
LR	Long rods	250 × 1500	797	1.17	1.05	0.05	0.05	8.6
γ -Al ₂ O ₃	—	—	178	0.39	0.32	—	—	9.1
NiMo/AS-SP	Spheres	3600 × 3600	500	0.60	0.60	0.01	0.02	5.5
NiMo/AS-HP	Hexagonal prisms	900 × 1000	403	0.59	0.56	0.02	0.04	6.9
NiMo/AS-SR	Short rods	350 × 1000	411	0.74	0.69	0.02	0.03	8.0
NiMo/AS-LR	Long rods	250 × 1300	387	0.71	0.67	0.01	0.01	8.5
NiMo/ γ -Al ₂ O ₃	—	—	133	0.31	0.28	—	—	8.8

^a Calculated by the BET method.^b The total pore volume was obtained at a relative pressure of 0.98.^c Calculated using the BJH method.^d Calculated using the *t*-plot method.^e Mesopore diameter calculated using the BJH method.**Fig. 7.** Raman spectra of different catalysts. (a) NiMo/AS-SP, (b) NiMo/AS-HP, (c) NiMo/AS-SR, (d) NiMo/AS-LR, (e) NiMo/ γ -Al₂O₃.

In addition, the broad band presented in NiMo/ γ -Al₂O₃ shifts to a lower value than those in NiMo/Al-SBA-15 catalysts with different morphologies, indicating a possible change in the coordination of Mo⁶⁺ species. The weak intensity of peak \sim 826 cm^{−1} is also associated with the orthorhombic MoO₃, suggesting the presence of a well-dispersed orthorhombic MoO₃ on the support surface. According to reference [51], the peak intensity of orthorhombic MoO₃ presented on NiMo/SBA-15 catalyst was high. Thus, the incorporation of Al atoms into the mesoporous framework seems to be favorable to the dispersion of MoO_x species on the support surface which will improve the HDS performance of the catalysts.

3.2.6. UV-Vis DRS of the oxide NiMo catalysts

UV-Vis diffuse reflectance spectroscopy was recorded in the wavelength range of 200–800 nm to further determine the nature of the coordination and aggregation state of Mo oxidic species in the catalysts with different morphologies and the results are shown in Fig. S4. In the spectra of each examined NiMo catalyst, the absorption in the 200–400 nm region should be associated to the ligand-to-metal charge transfer band (LMCT) O^{2−} → Mo⁶⁺ [52,53]. The exact positions of these bands depend strongly on the local coordination around Mo⁶⁺. In these spectra, none of the samples exhibit absorption at wavelengths longer than 350 nm, indicating that they have no aggregated MoO₃ species, but only highly dispersed Mo-oxides [54,55]. This is consistent with the Raman spectra and XRD results. According to reference [56], the bands in the lower wavelength region (260–280 nm) and in the higher

region (280–330 nm) are assigned to the isolated molybdate (tetrahedral) and polymolybdate (octahedral) species, respectively. Both types of Mo⁶⁺ species also show the second strong absorption band at about 230 nm. In Fig. S4, all the corresponding catalysts exhibit a mixture of Mo⁶⁺ oxidic species in tetrahedral and octahedral coordinations. These octahedron Mo species are more easy to form the coordinatively unsaturated or sulfur vacancies, which favor the hydrodesulfurization reaction. Among the Al-SBA-15-supported catalysts with different morphologies, NiMo/AS-SP with sphere morphology has the highest proportion of octahedral Mo⁶⁺ due to the high diffusivity of the active components in the spheres SBA-15 during the preparation of the catalysts. Therefore, the hydrodesulfurization properties of NiMo/AS-SP catalyst may be higher than the others.

3.2.7. Py-FTIR spectra of the oxide NiMo catalysts

It is well known that the acidity of the catalysts plays an important role in the hydrodesulfurization reaction [57,58]. To determine the strength and types of acid sites of these catalysts, pyridine IR spectroscopy measurements were performed at 200 and 350 °C. The pyridine adsorption IR spectra after degassing at 200 °C are assigned to the total amounts of acid sites, while the IR pyridine adsorption spectra after degassing at 350 °C are associated to the amounts of medium and strong acid sites. The band at 1540 cm^{−1} is attributed to pyridine adsorbed onto Brønsted acid sites, and the bands at 1450 and 1572 cm^{−1} are assigned to pyridine adsorbed onto Lewis acid sites, while the band at 1492 cm^{−1} is ascribed to a combination of Brønsted and Lewis acid sites [59–61]. Fig. S5 shows the FT-IR spectra of the catalysts after pyridine evacuation at 200 and 350 °C in the region of 1600–1400 cm^{−1}. It can be found that there are no Brønsted acid sites in the spectra of NiMo/ γ -Al₂O₃ since the absence of the IR absorption band of pyridinium at 1540 cm^{−1}. In Fig. S5A, the band at 1540 cm^{−1} presents in the spectra of NiMo/AS-SP, NiMo/AS-HP, and NiMo/AS-SR catalysts, indicating the existence of Brønsted acid sites on these catalysts. And the Lewis acid sites are found on all the catalysts.

Table 3 lists the acid strength distributions and the acid amounts of the catalysts which were quantitatively estimated using pyridine adsorption followed by degassing at 200 and 350 °C. After degassing at 200 °C, the total acidity (Brønsted + Lewis) of the series catalysts follows the order of NiMo/AS-SP > NiMo/AS-SR > NiMo/AS-HP > NiMo/AS-LR > NiMo/ γ -Al₂O₃, which is consistent with the result of the Si/Al ratios of the supports detected by XRF, where the Si/Al ratios of AS-SP, AS-SR, AS-HP, and AS-LR supports are 15.1, 16.3, 16.5, and 17.8, respectively. After degassing at 350 °C, the amounts of medium and strong acid sites of NiMo/AS-SP are slightly higher than that of NiMo/AS-SR, NiMo/AS-HP, NiMo/AS-LR, and NiMo/ γ -Al₂O₃. And the amounts of medium and strong

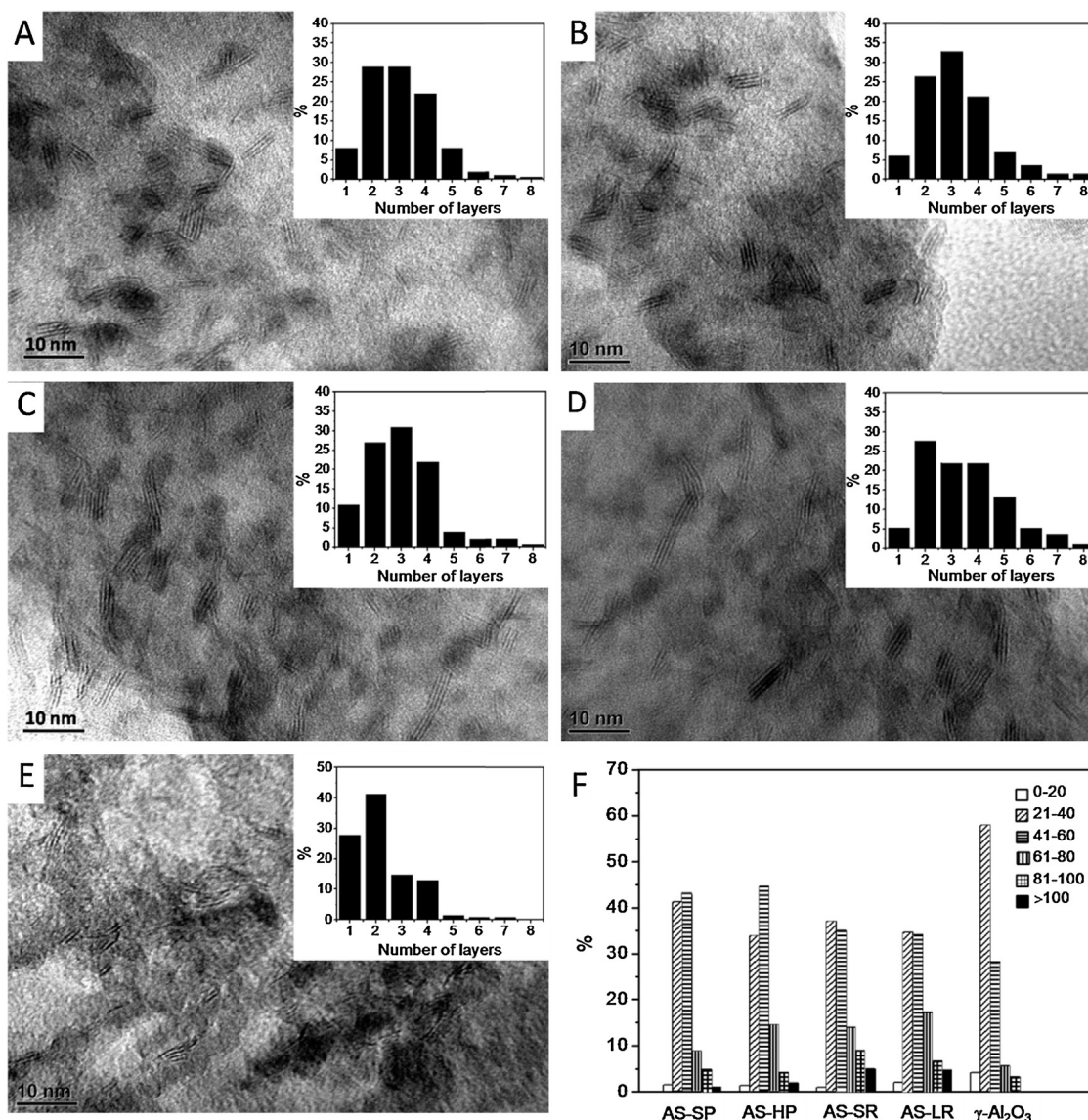


Fig. 8. HRTEM images of the sulfided catalysts (A) NiMo/AS-SP, (B) NiMo/AS-HP, (C) NiMo/AS-SR, (D) NiMo/AS-LR, (E) NiMo/ γ -Al₂O₃; (F) Number of length in Å of the MoS₂ particles dispersed on supported catalysts.

acid sites of NiMo/AS-SR, NiMo/AS-LR, and NiMo/ γ -Al₂O₃ are close to each other. The more acid sites and the lower Si/Al ratio of NiMo/AS-SP may be due to the easy diffusion of aluminum precursor to the mesochannels of sphere SBA-15 particles during grafting of alumina on SBA-15. Among all the catalysts, the proportion of Lewis acid sites is much larger than Brønsted acid sites. According to the above information, Al-grafted SBA-15 material brings small amounts of B acid sites and large amounts of Lewis acid sites in

Table 3
Amounts of B and L acid sites of the catalysts determined by pyridine-FTIR.

Sample	Amount of acid sites ($\mu\text{mol/g}$)					
	200 °C			350 °C		
	L	B	L+B	L	B	L+B
NiMo/AS-SP	135.9	15.0	150.9	80.1	—	80.1
NiMo/AS-HP	128.8	13.2	143.0	71.0	—	71.0
NiMo/AS-SR	131.8	11.9	143.7	75.4	—	75.4
NiMo/AS-LR	126.0	15.8	141.8	72.0	—	72.0
NiMo/ γ -Al ₂ O ₃	108.0	0	110.7	70.5	—	70.5

NiMo/AS-SP, NiMo/AS-HP, NiMo/AS-SR, and NiMo/AS-LR catalysts which favor to improve the catalytic performances.

3.2.8. HRTEM of the sulfided catalysts

HRTEM characterization of the sulfided catalysts was carried out to obtain the information about the dispersion of MoS₂ crystal-lites over the five catalysts. The representative HRTEM micrographs of the five sulfided catalysts and the corresponding length and layer number of MoS₂ are shown in Fig. 8. The stacking numbers and lengths of the MoS₂ slabs on the five catalysts were obtained through statistical analyses based on about 25 representative micrographs involving 300–400 MoS₂ slabs.

In Fig. 8E, the MoS₂ species of the sulfided NiMo/ γ -Al₂O₃ catalyst is less stacked, with the highest stacking layers around 1–2, which is unfavorable to the planar adsorption of the DBT molecules through the aromatic rings. The NiMo/ γ -Al₂O₃ catalyst contains much Mo–O–Al linkages with alumina related to the strong interaction between Mo and hydroxyl groups, indicating that the Mo species are not fully sulfided and have lower activity. Compared to NiMo/ γ -Al₂O₃, it can be seen from Fig. 8A–D that the length and layer number of MoS₂ slabs are high on

Table 4Average length (L_{av}) and average stacking number (N_{av}) of MoS₂ crystallites.

Catalyst	L_{av} (nm)	N_{av}
NiMo/AS-SP	4.9	2.9
NiMo/AS-HP	5.1	3.2
NiMo/AS-SR	5.2	3.1
NiMo/AS-LR	5.4	3.5
NiMo/ γ -Al ₂ O ₃	4.0	2.1

NiMo/AS-SP, NiMo/AS-HP, NiMo/AS-SR, and NiMo/AS-LR catalysts with the MoS₂ layer numbers focused on two, three, or four layers.

The results of the average length and number of layers of the MoS₂ slabs displayed in Table 4, showing that the average length and the stacking layer number of MoS₂ slabs in the sulfided NiMo/ γ -Al₂O₃ are 4.0 nm and 2.1, respectively. The average length of the MoS₂ slabs on the sulfided five catalysts follows the order NiMo/ γ -Al₂O₃ (4.0 nm) < NiMo/AS-SP (4.9 nm) < NiMo/AS-HP (5.1 nm) < NiMo/AS-SR (5.2 nm) < NiMo/AS-LR (5.4 nm). The average number of the MoS₂ slabs on the five catalysts follows the order: NiMo/ γ -Al₂O₃ (2.1) < NiMo/AS-SP (2.9) < NiMo/AS-SR (3.1) < NiMo/AS-HP (3.2) < NiMo/AS-LR (3.5), indicating that the MoS₂ slabs on the sulfided NiMo/AS-SP, NiMo/AS-HP, NiMo/AS-SR, and NiMo/AS-LR catalysts have larger average lengths and higher stackings than on the sulfided NiMo/ γ -Al₂O₃. And the dispersion degree of MoS₂ slabs on the Al-SBA-15-supported catalysts follows the order: NiMo/AS-LR < NiMo/AS-HP < NiMo/AS-SR < NiMo/AS-SP, which is consistent with the result of UV–Vis diffuse reflectance spectroscopy.

The Co(Ni)–Mo–S model is used widely to understand and controls the catalytic properties of hydrotreating catalysts. The Co(Ni)–Mo–S structure is present as either type I or type II depending on the nature of metal–support interactions, which have different catalytic properties [62]. The type I contains strong interactions between the Co(Ni)–Mo–S structures and the support, and has low intrinsic activity. If the interactions between the Co(Ni)–Mo–S structures and the support decrease, the structure is termed as the type II Co(Ni)–Mo–S phase, which has an improved intrinsic activity. The present research aims at optimizing the formation of type II Co(Ni)–Mo–S active phases [7]. The NiMo/ γ -Al₂O₃ shows strong interactions between the MoS₂ and the alumina support and has high dispersion of the Co(Ni)–Mo–S structures with most of active sites being of type I, which has low intrinsic hydrogenation ability. For NiMo/Al-SBA-15 catalysts, the interactions between the MoS₂ and the support decrease, then the stacking degrees are high and their active sites are existing as type II. It is important to note that only the top layer of multi-stacks will expose the special brim sites, which play a key role for hydrogenation reactions. Thus, if the stacking degree of MoS₂ is too high, the number of brim sites will reduce, and therefore it will be difficult to proceed the sulfur elimination via the perpendicular adsorption of the reactant molecule through the S atom [63]. According to the results of the average length and number of layers of the MoS₂ slabs displayed in Table 4, the sphere NiMo/AS-SP catalyst has compromised dispersion and stacking of MoS₂ slabs, creating more type II active sites with more brim active sites than the other catalysts.

3.3. Catalytic activity

The activities of NiMo series catalysts supported on Al-SBA-15 with different morphologies were determined in the HDS of DBT. The HDS conversions of DBT over the catalysts under different reaction temperatures at the weight time of 2.77 and 0.15 g min mol^{−1} are present in Figs. 9 and 10, respectively. From Fig. 9, it can be found that the DBT conversions of all the catalysts increase with the reaction temperature increased at the weight time of 2.77 g min mol^{−1},

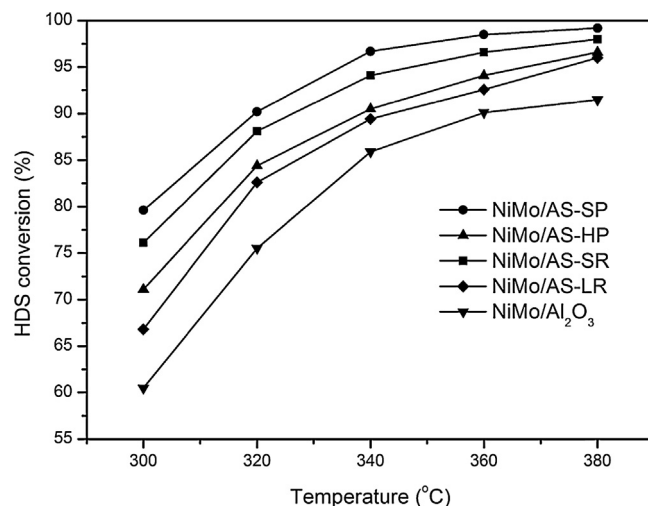


Fig. 9. Conversions of DBT in the HDS reaction over the catalysts at different temperatures with the weight time of 2.77 g min mol^{−1}.

and they were all higher than 96% at 380 °C. Furthermore, the conversion of DBT in the HDS reaction over different catalysts follows the order: NiMo/ γ -Al₂O₃ < NiMo/AS-LR < NiMo/AS-HP < NiMo/AS-SR < NiMo/AS-SP. The NiMo/AS-SP catalyst shows the highest DBT conversion at all the reaction temperatures, and its DBT conversion is much higher than that of NiMo/AS-LR catalyst. The higher activity of the catalyst NiMo/AS-SP with sphere morphology can be explained by which all of the external surfaces over the sphere SBA-15 mesoporous material distribute with mesopore cavities, which make the internal surface have high connectivity and the active component MoS₂ have high dispersion. Thus DBT molecules can diffuse in and out of the mesochannels from each side of the catalyst and have higher conversion. In comparison to the spheres SBA-15, the hexagonal prisms and rods SBA-15 have higher aspect ratios, and the mesochannel orifices of which only exist at both ends, indicating that the internal surface of mesochannels are not easy to be contacted and the MoS₂ have poor dispersion in the internal surface of SBA-15. Then the conversions of DBT molecules in the hexagonal prisms and rods SBA-15 are inferior to the spheres SBA-15. In addition, it is obvious from Fig. 10 that the DBT conversions of the catalysts at the weight time of 0.15 g min mol^{−1} follow the same order with that of the reaction weight time of 2.77 g min mol^{−1},

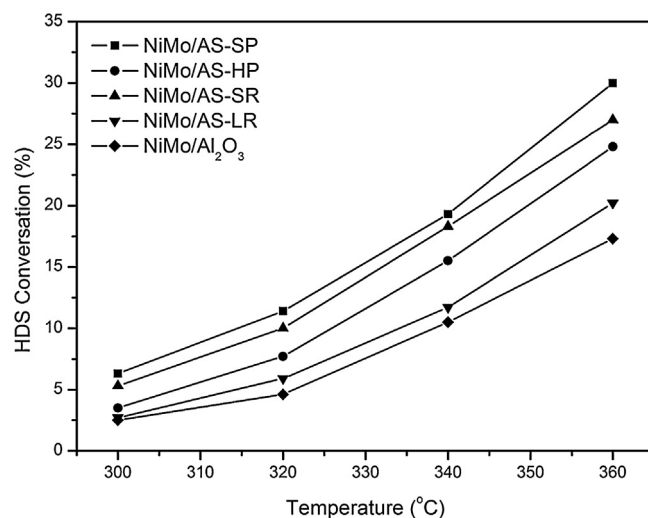


Fig. 10. Conversions of DBT in the HDS reaction over the catalysts at different temperatures with the weight time of 0.15 g min mol^{−1}.

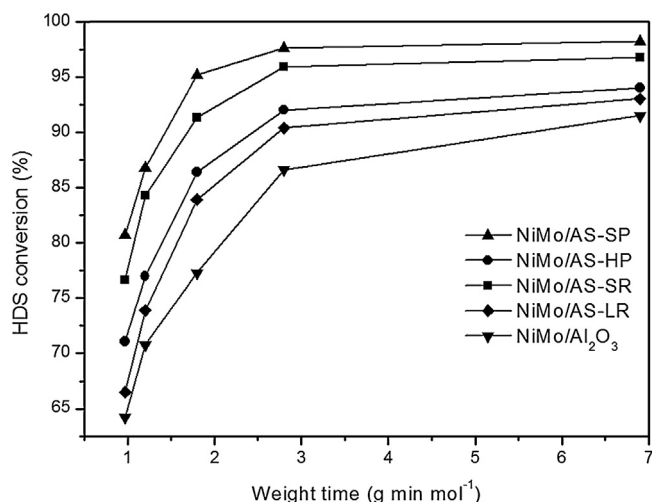


Fig. 11. Conversions of DBT in the HDS reaction over different catalysts as a function of weight time.

but the conversions of DBT are comparatively lower. For example, the conversions of DBT over all the catalysts were below 30% at different temperatures. NiMo/ γ -Al₂O₃ exhibited the lowest activity with the conversion of DBT below 3% at the reaction temperature of 300 °C. It can be concluded that the morphologies and mesochannels of SBA-15 have an important influence on the hydrodesulfurization properties of NiMo catalysts.

The DBT HDS performance of NiMo-supported catalysts with different morphologies were also evaluated at different weight times and 340 °C, and the results are shown in Fig. 11. It can be seen from Fig. 11 that the conversions of DBT in the HDS reaction over the catalysts with different morphologies at all weight times follow the order NiMo/ γ -Al₂O₃ < NiMo/AS-LR < NiMo/AS-HP < NiMo/AS-SR < NiMo/AS-SP. During the process of HDS reaction, the increase in weight time results in a sharp increase of DBT conversion, especially as the weight time lower than 2.8 g min mol⁻¹. The DBT conversion over NiMo/AS-SP catalyst is 80.7% at τ = 0.97 g min mol⁻¹, much higher than the conversion over NiMo/AS-LR (66.5%). At high weight time (τ = 6.9 g min mol⁻¹), the conversion of DBT over NiMo/AS-SP catalyst is as high as 98.2%, and even higher than NiMo/AS-LR (93.0%), demonstrating that the support morphology has a significant influence on the DBT conversion with the increase of weight time.

Fig. 12 shows the product distributions in the HDS of DBT on NiMo/AS-SP catalyst as a function of weight time and reaction temperature at 340 °C. It can be achieved from Fig. 12 that the high weight time can favor the HDS reaction rate of DBT through DDS route rather than via the HYD route, reflected by the increased selectivity of biphenyl (BP) and the decreased selectivity of cyclohexylbenzene (CHB). It can be obtained that there is some limits for the HYD route at high weight time. Among all the final products, biphenyl (BP) is always the most abundant products at different reaction weight times. The selectivity of biphenyl (BP) is about 58.0% at low weight time and 68.4% at high weight time, indicating that the DDS pathway is the main reaction pathway of DBT HDS over the NiMo/AS-SP catalyst. The DBT conversion increases at high weight time mainly due to the increase in biphenyl (BP) yield. The selectivities of all the products are changing sharply with the increase in weight time from 0.97 to 2.8 g min mol⁻¹, while the selectivities change slightly as the weight time is higher than 2.8 g min mol⁻¹. The selectivities to form cyclopentylmethylbenzene (CPMB), cyclohexenylbenzene (CHEB), and dicyclohexyl (DCH) increase with the

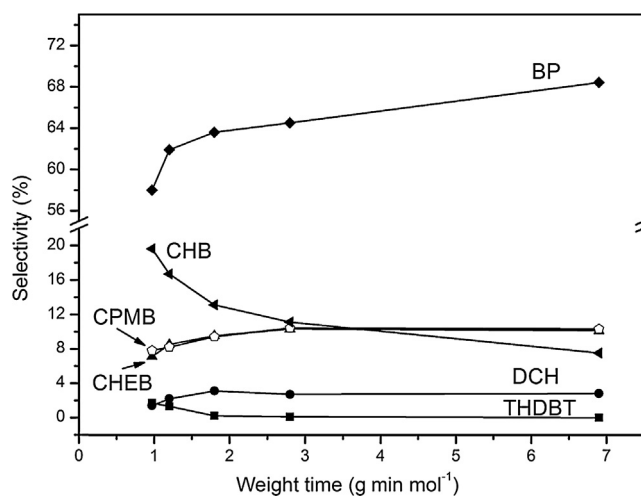


Fig. 12. Product distributions in the HDS of DBT on NiMo/AS-SP catalyst as a function of weight time.

increasing weight time, while the selectivity to tetrahydrodibenzothiothiophene (THDBT) decreases with the increase of weight time.

The DBT HDS performance of the NiMo/AS-SP was evaluated under different temperatures and the weight time at 2.8 g min mol⁻¹. The final product distributions identified by GC-MS are shown in Fig. 13. It can be found that the selectivity to BP increases with increasing reaction temperature, while the selectivity to CHB decreases, indicating that high temperature can facilitate the HDS reaction via the DDS route more than via the HYD reaction. In the range of the reaction temperatures from 300 to 380 °C, BP is the main product of the hydrodesulfurization products of DBT over NiMo/AS-SP catalyst, demonstrating that the DDS pathway is the main reaction pathway of DBT HDS. As the reaction temperature is higher than 340 °C, the selectivity to THDBT and the adsorption rate of the reactants over the catalyst decrease, confirming that the HYD route of DBT is only favored at low temperature. The HYD pathway of DBT is found to be thermodynamically limited to some extent as Bao [7] reported in the previous studies. In addition, the selectivity to CHB decreases with temperature, while the selectivity to CHEB increases, which is probably due to the shift of equilibrium from CHB to CHEB at high reaction temperatures. The selectivity to DCH fluctuates with the increase in temperature, which is due to the interaction between the two pathways of DBT HDS over the

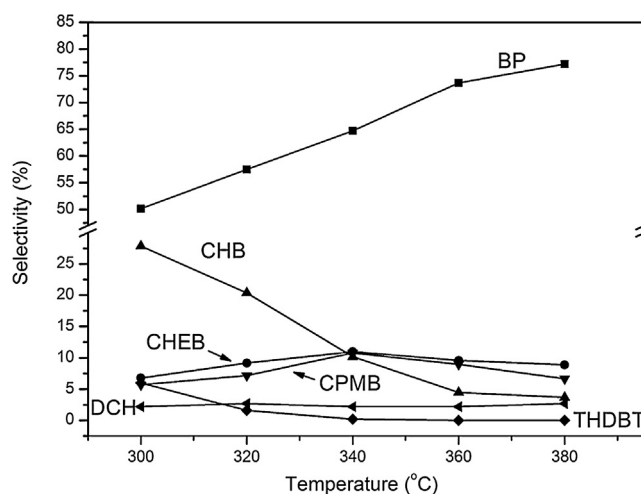


Fig. 13. Selectivity of the final products over NiMo/AS-SP catalyst for DBT HDS at different temperatures.

catalyst. It can be concluded that both HYD and DDS pathways play important roles in the DBT HDS.

4. Discussion

4.1. Effect of the morphology of Al-SBA-15 on the catalytic performance for DBT HDS

The catalytic performances of DBT HDS over these catalysts are closely related to their physicochemical properties of the supports, the dispersion of the active metals, and the acid properties of the catalysts. Among these influence factors, the morphology and mesochannel of Al-SBA-15 mesoporous materials are the crucial factors for DBT HDS reaction. Simple morphologies with short unhindered path lengths, such as small spheres, crystal-like particles, and short straight rods, are beneficial for eliminating the diffusion resistance [29]. In this research, four catalysts with spheres, hexagonal prisms, short rods, and long rods morphologies were studied to clarify the relationship between the catalytic performances and their morphologies.

The results of SEM, TEM, XRD, N_2 adsorption–desorption, HRTEM, and Py-FTIR analyses have shown that the sphere SBA-15 support has mesoporous orifices on each place of the spherical surface with the pore diameter of 5.8 nm. The mesochannel orifices of the hexagonal prisms and rods SBA-15 only exist at both of the ends. The mesochannels are highly ordered and stacked along the long axis direction of the hexagonal prisms, short rods, and long-rod SBA-15 with the diameters of 7.4, 8.2, and 8.6 nm, respectively. The morphology and mesochannel of SBA-15 mesoporous materials play an important role in the dispersion of the active metals and the acid properties of the catalysts. According to the results of the rate constant k_{HDS} , TOF, HYD/DDS ratios, and other kinetic parameters of different catalysts for DBT HDS listed in Table 5, it can be found that the catalyst NiMo/AS-SP shows the highest TOF and rate constant, while the TOF of NiMo/ γ - Al_2O_3 is the lowest. The DBT HDS activities for the NiMo-supported Al-SBA-15 catalysts follow the order: NiMo/AS-LR < NiMo/AS-HP < NiMo/AS-SR < NiMo/AS-SP. The best performance of NiMo/AS-SP can be correlated to the good diffusivity of DBT and the suitable dispersions of MoS_2 in the sphere Al-SBA-15 material compared with other morphologies of Al-SBA-15. Moreover, the pore size of long-rod catalyst (8.5 nm) is larger than that of hexagonal prism (6.9 nm) and short-rod catalyst (8.0 nm), the length of mesochannels over NiMo/AS-LR (1300 nm) is also longer than that of hexagonal prism (1000 nm) and short-rod catalyst (1000 nm). These results demonstrate that NiMo/AS-LR exhibits the poor performance for DBT HDS due to its longer mesochannels. In addition, the average length of the hexagonal prism and short-rod catalysts are similar with each other, while the pore size of mesochannels of short-rod catalyst is larger than that of the hexagonal prism catalyst. Therefore, the diffusion of DBT molecules and active component MoS_2 in the short-rod catalyst can be easier than the hexagonal prism catalyst. And the activity of DBT HDS over NiMo/AS-SR is better than NiMo/AS-HP. The schematic representation of the reaction of DBT molecules on NiMo-supported Al-SBA-15 catalysts with different morphologies is presented in Fig. S6.

Over the above studied catalysts, the preferential HDS route is the DDS pathway, while the preferential HDS route over NiMo/ γ - Al_2O_3 is the HYD pathway. The higher selectivity to BP over the NiMo supported on Al-SBA-15 catalysts indicates that all of the as-synthesized NiMo Al-SBA-15 catalysts with different morphologies have better hydrogenolysis desulfurization activities than the conventional NiMo/ γ - Al_2O_3 catalyst. These results can be correlated to the different contents of Brønsted and Lewis acid sites of the catalysts and different morphologies of MoS_2 on the surface

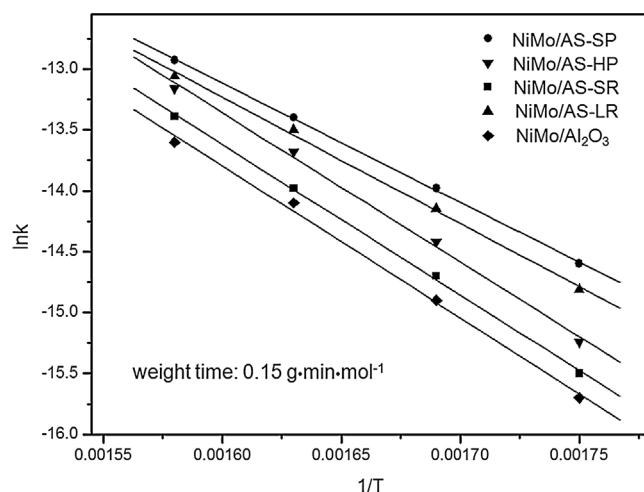


Fig. 14. Arrhenius plots for DBT HDS over the five catalysts.

of the sulfided catalysts. The enhanced Brønsted acid sites on Al-SBA-15 support can improve the DDS pathway and thus result in an increased DBT HDS efficiency [57].

Fig. 14 shows the Arrhenius plots for DBT HDS at the DBT conversion <30% (at which the temperature range was 300–360 °C) over the five catalysts. According to the slopes of the linear Arrhenius plots, the values of active energy, E_a , for DBT HDS over different catalysts can be calculated, and the results are shown in Table 5. It can be found that the E_a value (81.4 kJ/mol) of the catalyst NiMo/AS-SP is the lowest one among these catalysts, while the NiMo/ γ - Al_2O_3 catalyst exhibits the highest E_a value (103.8 kJ/mol). The E_a values follow the order: NiMo/AS-SP < NiMo/AS-SR < NiMo/AS-HP < NiMo/AS-LR < NiMo/ γ - Al_2O_3 . According to the previous studies [41], the lower the E_a value is, the higher the conversion of DBT HDS over the catalysts. Different values of E_a over these catalysts may have high correlation to their morphologies of different supports and different contents of Brønsted and Lewis acid sites over the catalysts. Fig. S7 shows the Eyring plots for DBT HDS over the five catalysts. From the linear relationship between $\ln(k/T)$ and $1/T$, the activation entropy and enthalpy could be calculated, and the results are summarized in Table 5. It can be seen from Table 5 that the activation enthalpy values of the DBT HDS reactions are positive, indicating that these reactions are endothermic [40]. The activation enthalpy values increase with the sequence of NiMo/AS-SP < NiMo/AS-SR < NiMo/AS-LR < NiMo/AS-HP < NiMo/ γ - Al_2O_3 catalyst. The NiMo/AS-SP catalyst, which has the lowest activation enthalpy value, exhibits a more rapid reaction rate for DBT HDS at lower temperature. The entropy of DBT HDS over these catalysts follows the same order with the activation enthalpy of them. Therefore, the kinetic investigations confirm that NiMo/AS-SP exhibits a good catalytic performance for DBT HDS.

4.2. Reaction network of DBT HDS over the NiMo/Al-SBA-15 catalysts

The product distributions in the HDS of DBT over the supported catalysts of NiMo/AS-SP, NiMo/AS-HP, NiMo/AS-SR, NiMo/AS-LR, and NiMo/ γ - Al_2O_3 are shown in Table 6. Eight products were detected over the Al-SBA-15 supported NiMo catalysts with different morphologies, while only five products were detected on NiMo/ γ - Al_2O_3 catalyst. Similar to the previous reports [7], no lighter cracking products of DBT HDS was detected over NiMo supported on Al-SBA-15 catalysts, meaning that no secondary cracking reactions occurred on the catalysts. The HDS products of DBT were identified by GC-MS chromatograph as shown in Fig. S8. It

Table 5Rate constant k_{HDS} , TOF, HYD/DDS ratios and kinetic parameters obtained over different catalysts for DBT HDS at 340 °C.

Catalyst	k_{HDS}^a ($10^{-6} \text{ mol g}^{-1} \text{ s}^{-1}$)	TOF ^b (10^3 s^{-1})	HYD/DDS ratio ^c	E_a^d (kJ mol ⁻¹)	ΔH^e (kJ mol ⁻¹)	ΔS^f (J mol ⁻¹ K ⁻¹)
NiMo/AS-SP	1.45	6.02	0.34	81.4	75.5	-239.4
NiMo/AS-HP	1.15	5.35	0.28	102.0	97.3	-206.5
NiMo/AS-SR	1.37	5.77	0.38	86.2	81.3	-231.0
NiMo/AS-LR	0.85	4.99	0.29	103.1	96.8	-209.5
NiMo/ γ -Al ₂ O ₃	0.73	3.36	0.72	103.8	102.6	-199.2

^a Reaction rate constant in mol g⁻¹ s⁻¹.^b Number of reacted DBT molecules per hour and per Mo atom at the edge surface.^c Calculated by dividing the BP selectivity into the CHB selectivity at the DBT HDS conversion of 50%.^d Calculated using Arrhenius equation.^e Calculated using Eyring equations.^f Calculated using Eyring equations.**Table 6**

Selectivity of the final products over the different catalysts for DBT HDS at 340 °C.

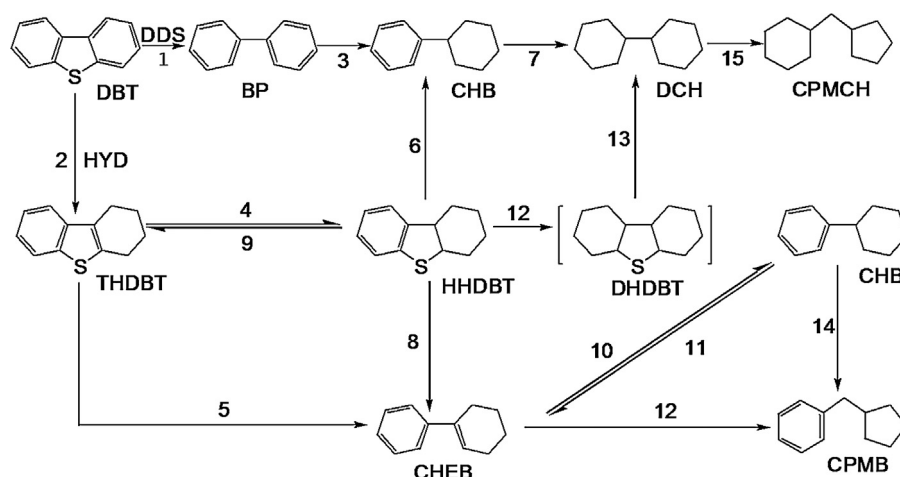
Selectivity (%) ^a	NiMo/AS-SP	NiMo/AS-HP	NiMo/AS-SR	NiMo/AS-LR	NiMo/ γ -Al ₂ O ₃
BP	64.4	67.5	67.1	66.2	54.0
CHEB	11.0	10.7	10.0	9.3	0.2
CHB	10.2	9.6	9.8	12.7	39.1
DCH	2.2	2.9	2.5	2.2	4.8
THDBT	0.2	0.6	0.4	0.4	1.9
CPMCH	0.9	0.8	0.8	0.9	0
HHDBT	0.1	0.3	0.2	0.1	0
CPMB	10.8	7.9	9.4	8.2	0

^a The selectivity data were calculated from the GC-MS analysis results which is just a semiquantitative method.

is well known that there are two pathways for DBT HDS reaction [64,65]. The first one is called direct desulfurization route (DDS), sulfur elimination via hydrogenolysis of C–S bonds, yielding biphenyl (BP); the second one is the hydrogenation pathway (HYD), desulfurization proceeded after hydrogenation of one of the aromatic rings of DBT molecule, yielding the products of tetrahydrodibenzothiophene (THDBT), cyclohexenylbenzene (CHEB), and cyclohexylbenzene (CHB). All of the above products were detected on NiMo/ γ -Al₂O₃ catalyst as reported by Wang and Prins [66]. In addition, for the NiMo-supported Al-SBA-15 catalysts, the hexahydrodibenzothiophene (HHDBT) and cyclopentyl-methylbenzene (CPMB) were also detected in the final products as Bao reported [7]. The absence of HHDBT in the products over NiMo/ γ -Al₂O₃ may be due to the fast desulfurization of HHDBT in the reaction processes. Under the reaction temperature at 340 °C, the selectivities of BP and CHEB over all the NiMo-supported Al-SBA-15 catalysts were much higher than NiMo/ γ -Al₂O₃ while the selectivity of CHB was lower than the latter. It can be seen from the results in Table 6 that there are no big differences between these NiMo-supported

Al-SBA-15 catalysts with different morphologies in terms of HDS product selectivity of the reactant DBT due to their similar Brønsted and Lewis acidities.

Combining the results reported in the previous studies [7] and in the above discussions, the possible reaction network of DBT HDS over the NiMo series catalysts supported on Al-SBA-15 catalysts with different morphologies is represented in Fig. 15. Reactions 1–7 are the typical processes in the DBT HDS reactions over NiMo/ γ -Al₂O₃ catalyst, and more reaction processes occur on the NiMo/Al-SBA-15 catalysts, since the amounts of Brønsted and Lewis acid sites of NiMo/Al-SBA-15 catalysts are much higher than that of NiMo/ γ -Al₂O₃. As previous reported [67], these acid sites can promote the hydrogenolysis and isomerization activities of the catalysts. For all these catalysts studied, the hydrogenation of the first phenyl ring is the rate-controlling step in the HYD pathway, and the desulfurization of the partially hydrogenated intermediates is relatively fast due to the low yields of the intermediates. Although HHDBT was not detected over NiMo supported on Al-SBA-15 catalysts due to the fast conversion of HHDBT, the reactions

**Fig. 15.** Possible reaction network of DBT HDS over NiMo supported on Al-SBA-15 catalysts with different morphologies.

12 and 13 may also exist in the HDS reaction processes. Due to a certain amount of Brønsted acid sites existing in NiMo supported on Al-SBA-15 catalysts, the product CPMB can be obtained from the isomerization reactions of CHB and CHEB. The selectivity to BP increases slightly with the increase of weight time, indicating that the hydrogenation of BP to CHB is difficult to proceed. The hydrogenation of the second phenyl ring of CHB to DCH is more difficult since the selectivity to DCH is very low under the reaction conditions. In addition, the isomerization reaction of DCH to CPMCH might also occur on the Brønsted acid sites of the catalysts.

5. Conclusions

Mesoporous SBA-15 silicas with spheres, hexagonal prisms, short rods, and long rods morphologies were synthesized via a facile method. Moreover, highly ordered mesoporous Al-SBA-15 with a Si/Al molar ratio of 10 had been synthesized via three different post-synthesis routes. The characterization results showed that alumination by reacting SBA-15 silica wall surfaces with alumina chloride in dry ethanol can maintain the surface area and porous structure of the SBA-15. After impregnation of Ni and Mo active metals, the morphology and two-dimensional hexagonal (*p6mm*) structure of SBA-15 remained. The sulfided sphere NiMoS₂/AS-SP catalysts had the appropriate dispersions and stacking numbers of MoS₂ slabs which provided more brim active sites for the DBT HDS than other catalysts.

Among these catalysts, the sphere catalyst (NiMo/AS-SP) showed the highest TOF and rate constant, and its DBT conversion was much higher than the long-rod catalyst (NiMo/AS-LR). The higher activity of the catalyst with sphere morphology could be correlated to its suitable mesochannels and the high dispersion of the active component MoS₂ on the sphere SBA-15 mesoporous material. In comparison to the spheres SBA-15, the mesochannel orifices of the hexagonal prisms and rods SBA-15 only existed at both of the ends, indicating a poor diffusion performance of DBT. Furthermore, the pore size of the long-rod catalyst was larger than that of the hexagonal prism and the short-rod catalyst, and the length of mesochannels on NiMo/AS-LR was also longer than that of hexagonal prism and short-rod catalyst. Moreover, the average lengths of the hexagonal prism and short-rod catalysts were similar with each other, while the pore size of the mesochannels over the short-rod catalyst was larger than that of the hexagonal prism catalyst. And the characterization results showed that the dispersion degrees of MoS₂ slabs on the Al-SBA-15-supported catalysts and the diffusivities of DBT molecules in different morphology catalysts followed the order: NiMo/AS-LR < NiMo/AS-HP < NiMo/AS-SR < NiMo/AS-SP, which was consistent with the activity of DBT HDS over these catalysts.

The DBT HDS over NiMo supported on Al-SBA-15 catalysts with different morphologies had similar reaction network. The enhanced Brønsted and Lewis acid sites of NiMo/Al-SBA-15 can favor the hydrogenolysis/isomerization performance of the catalysts, and the isomerization products CPMB and CPMCH were detected over NiMo/Al-SBA-15 catalysts. Among these catalysts, the HYD pathway was the preferential HDS route over NiMo/ γ -Al₂O₃, while the preferential HDS route over the NiMo-supported Al-SBA-15 catalysts was the DDS pathway due to the adjustable acidity of the NiMo/Al-SBA-15 catalysts.

Acknowledgements

The authors acknowledge the financial supports from the NNSFC (Nos. 21276277, 21173269 and 91127040), Specialized Research Fund for the Doctoral Program of Higher Education (20130007110003), and Opening Project of Guangxi Key

Laboratory of PRPPIT (2012K01). The open funds of the State Key Laboratory of Chemical Resource Engineering and the State Key Laboratory of Inorganic Synthesis and Preparative Chemistry.

Appendix A. Supplementary data

Supplementary data associated with this article can be found, in the online version, at <http://dx.doi.org/10.1016/j.apcatb.2014.10.034>.

References

- [1] C. Song, X. Ma, *Applied Catalysis B: Environmental* 41 (2003) 207–238.
- [2] D. Zhang, A. Duan, Z. Zhao, C. Xu, *Journal of Catalysis* 274 (2010) 273–286.
- [3] F. Trejo, M.S. Rana, J. Ancheyta, *Catalysis Today* 130 (2008) 327–336.
- [4] F. Bataille, J.-L. Lemberon, P. Michaud, G. Pérot, M. Vrinat, M. Lemaire, E. Schulz, M. Breyse, S. Kasztelan, *Journal of Catalysis* 191 (2000) 409–422.
- [5] Y. Fan, G. Shi, H. Liu, X. Bao, *Applied Catalysis B: Environmental* 91 (2009) 73–82.
- [6] K. Soni, B.S. Rana, A.K. Sinha, A. Bhaumik, M. Nandi, M. Kumar, G.M. Dhar, *Applied Catalysis B: Environmental* 90 (2009) 55–63.
- [7] Y. Li, D. Pan, C. Yu, Y. Fan, X. Bao, *Journal of Catalysis* 286 (2012) 124–136.
- [8] D. Zhao, J. Feng, Q. Huo, N. Melosh, G.H. Fredrickson, B.F. Chmelka, G.D. Stucky, *Science* 279 (1998) 548–552.
- [9] D. Zhao, Q. Huo, J. Feng, B.F. Chmelka, G.D. Stucky, *Journal of the American Chemical Society* 120 (1998) 6024–6036.
- [10] A. Romero-Pérez, A. Infantes-Molina, E. Rodríguez-Castellón, A. Jiménez-López, *Applied Catalysis B: Environmental* 97 (2010) 257–268.
- [11] P. Biswas, B. Narayanasarma, C.M. Kotikalapudi, A.K. Dalai, J. Adjaye, *Industrial and Engineering Chemistry Research* 50 (2011) 7882–7895.
- [12] R. Huirache-Acuña, B. Pawelec, E. Rivera-Muñoz, R. Nava, J. Espino, J.L.G. Fierro, *Applied Catalysis B: Environmental* 92 (2009) 168–184.
- [13] K.-S. Cho, Y.-K. Lee, *Applied Catalysis B: Environmental* 147 (2014) 35–42.
- [14] J. Perez-Ramirez, C.H. Christensen, K. Egeblad, C.H. Christensen, J.C. Groen, *Chemical Society Reviews* 37 (2008) 2530–2542.
- [15] M. Baca, E. de la Rochefoucauld, E. Ambrose, J.-M. Krafft, R. Hajjar, P.P. Man, X. Carrier, J. Blanchard, *Microporous and Mesoporous Materials* 110 (2008) 232–241.
- [16] G. Muthu Kumaran, S. Garg, K. Soni, M. Kumar, J.K. Gupta, L.D. Sharma, K.S. Rama Rao, G. Murali Dhar, *Microporous and Mesoporous Materials* 114 (2008) 103–109.
- [17] P. Topka, J. Karban, K. Soukup, K. Jiráková, O. Šolcová, *Chemical Engineering Journal* 168 (2011) 433–440.
- [18] Y. Kanda, T. Aizawa, T. Kobayashi, Y. Uemichi, S. Namba, M. Sugioka, *Applied Catalysis B: Environmental* 77 (2007) 117–124.
- [19] Z. Luan, M. Hartmann, D. Zhao, W. Zhou, L. Kevan, *Chemistry of Materials* 11 (1999) 1621–1627.
- [20] S. Badoga, K.C. Mouli, K.K. Soni, A.K. Dalai, J. Adjaye, *Applied Catalysis B: Environmental* 125 (2012) 67–84.
- [21] M.Á. Calderón-Magdaleno, J.A. Mendoza-Nieto, T.E. Klimova, *Catalysis Today* 220–222 (2014) 78–88.
- [22] I. Agirrezabal-Telleria, J. Requies, M.B. Güemez, P.L. Arias, *Applied Catalysis B: Environmental* 115–116 (2012) 169–178.
- [23] A. Sayari, B.-H. Han, Y. Yang, *Journal of the American Chemical Society* 126 (2004) 14348–14349.
- [24] A. Katiyar, S. Yadav, P.G. Smirniotis, N.G. Pinto, *Journal of Chromatography A* 1122 (2006) 13–20.
- [25] S.-Y. Chen, C.-Y. Tang, W.-T. Chuang, J.-J. Lee, Y.-L. Tsai, J.C.C. Chan, C.-Y. Lin, Y.-C. Liu, S. Cheng, *Chemistry of Materials* 20 (2008) 3906–3916.
- [26] Y. Zhu, H. Li, J. Xu, H. Yuan, J. Wang, X. Li, *CrystEngComm* 13 (2011) 402.
- [27] Y. Wang, F. Zhang, Y. Wang, J. Ren, C. Li, X. Liu, Y. Guo, Y. Guo, G. Lu, *Materials Chemistry and Physics* 115 (2009) 649–655.
- [28] H. Wan, L. Liu, C. Li, X. Xue, X. Liang, *Journal of Colloid and Interface Science* 337 (2009) 420–426.
- [29] H.I. Lee, J.H. Kim, G.D. Stucky, Y. Shi, C. Pak, J.M. Kim, *Journal of Materials Chemistry* 20 (2010) 8483.
- [30] X. Ji, K.T. Lee, M. Monjauez, L.F. Nazar, *Chemical Communications* (2008) 4288–4290.
- [31] F. Cucinotta, F. Carniato, G. Paul, S. Bracco, C. Bisio, S. Caldarelli, L. Marchese, *Chemistry of Materials* 23 (2011) 2803–2809.
- [32] Y. Kang, C.B. Murray, *Journal of the American Chemical Society* 132 (2010) 7568–7569.
- [33] J. Yu, Y. Yu, P. Zhou, W. Xiao, B. Cheng, *Applied Catalysis B: Environmental* 156–157 (2014) 184–191.
- [34] X. Lin, Y. Fan, Z. Liu, G. Shi, H. Liu, X. Bao, *Catalysis Today* 125 (2007) 185–191.
- [35] Y. Sun, R. Prins, *Journal of Catalysis* 267 (2009) 193–201.
- [36] G. Berhault, M. Perez De la Rosa, A. Mehta, M.J. Yácamán, R.R. Chianelli, *Applied Catalysis A: General* 345 (2008) 80–88.
- [37] E.J.M. Hensen, P.J. Kooyman, Y. van der Meer, A.M. van der Kraan, V.H.J. de Beer, J.A.R. van Veen, R.A. van Santen, *Journal of Catalysis* 199 (2001) 224–235.
- [38] S. Kasztelan, H. Toulhoat, J. Grimbolt, J.P. Bonnelle, *Applied Catalysis* 13 (1984) 127–159.
- [39] O.Y. Gutiérrez, T. Klimova, *Journal of Catalysis* 281 (2011) 50–62.

- [40] M.A. Rodríguez, I. Elizalde, J. Ancheyta, *Fuel* 100 (2012) 152–162.
- [41] M.L. Vrinat, *Applied Catalysis* 6 (1983) 137–158.
- [42] T. Klimova, J. Reyes, O. Gutiérrez, L. Lizama, *Applied Catalysis A: General* 335 (2008) 159–171.
- [43] C. Suresh, D. Santharaj, M. Gurulakshmi, G. Deepa, M. Selvaraj, N.R. Sasi Rekha, K. Shanthi, *ACS Catalysis* 2 (2011) 127–134.
- [44] M. Gómez-Cazalilla, J.M. Mérida-Robles, A. Gurbani, E. Rodríguez-Castellón, A. Jiménez-López, *Journal of Solid State Chemistry* 180 (2007) 1130–1140.
- [45] I. Hannus, Z. Kónya, J.B. Nagy, P. Lentz, I. Kiricsi, *Applied Catalysis B: Environmental* 17 (1998) 157–166.
- [46] X. Liu, X. Li, Z. Yan, *Applied Catalysis B: Environmental* 121–122 (2012) 50–56.
- [47] X. Zhou, A. Duan, Z. Zhao, Y. Gong, H. Wu, J. Li, Y. Wei, G. Jiang, J. Liu, Y. Zhang, *Journal of Materials Chemistry A* (2014).
- [48] H. Shimada, T. Sato, Y. Yoshimura, J. Hiraishi, A. Nishijima, *Journal of Catalysis* 110 (1988) 275–284.
- [49] K. Otto, C.P. Hubbard, W.H. Weber, G.W. Graham, *Applied Catalysis B: Environmental* 1 (1992) 317–327.
- [50] P. Rayo, M.S. Rana, J. Ramírez, J. Ancheyta, A. Aguilar-Elguézabal, *Catalysis Today* 130 (2008) 283–291.
- [51] T.E. Klimova, D. Valencia, J.A. Mendoza-Nieto, P. Hernández-Hipólito, *Journal of Catalysis* 304 (2013) 29–46.
- [52] T. Klimova, L. Peña, L. Lizama, C. Salcedo, O.Y. Gutiérrez, *Industrial and Engineering Chemistry Research* 48 (2008) 1126–1133.
- [53] L. Lizama, T. Klimova, *Applied Catalysis B: Environmental* 82 (2008) 139–150.
- [54] T. Klimova, M. Calderón, J. Ramírez, *Applied Catalysis A: General* 240 (2003) 29–40.
- [55] M. Cheng, F. Kumata, T. Saito, T. Komatsu, T. Yashima, *Applied Catalysis A: General* 183 (1999) 199–208.
- [56] G. Xiong, Z. Feng, J. Li, Q. Yang, P. Ying, Q. Xin, C. Li, *The Journal of Physical Chemistry B* 104 (2000) 3581–3588.
- [57] Y. Ding, J. Liang, Y. Fan, Y. Wang, X. Bao, *Catalysis Today* 125 (2007) 178–184.
- [58] W.J.J. Welters, V.H.J. de Beer, R.A. van Santen, *Applied Catalysis A: General* 119 (1994) 253–269.
- [59] J.A.Z. Pieterse, S. Veefkind-Reyes, K. Seshan, L. Domokos, J.A. Lercher, *Journal of Catalysis* 187 (1999) 518–520.
- [60] T. Kataoka, J.A. Dumesic, *Journal of Catalysis* 112 (1988) 66–79.
- [61] T. Zhang, J. Liu, D. Wang, Z. Zhao, Y. Wei, K. Cheng, G. Jiang, A. Duan, *Applied Catalysis B: Environmental* 148–149 (2014) 520–531.
- [62] H. Topsøe, *Applied Catalysis A: General* 322 (2007) 3–8.
- [63] C. Song, *Catalysis Today* 86 (2003) 211–263.
- [64] M. Egorova, R. Prins, *Journal of Catalysis* 225 (2004) 417–427.
- [65] H. Kim, J.J. Lee, S.H. Moon, *Applied Catalysis B: Environmental* 44 (2003) 287–299.
- [66] H. Wang, R. Prins, *Journal of Catalysis* 258 (2008) 153–164.
- [67] D. Li, T. Sato, M. Imamura, H. Shimada, A. Nishijima, *Applied Catalysis B: Environmental* 16 (1998) 255–260.